

1 **FULLY COUPLED FLOW-LIQUEFACTION IN TAILINGS STORAGE FACILITIES:**  
 2 **INDUCED SHEAR BANDWIDTH ON PARTIALLY DRAINED TRIGGERS.**

3 NICOLAS A. LABANDA<sup>‡</sup>, FELIPE LOPEZ RIVAROLA<sup>\*</sup>, NICOLAS TASSO<sup>†</sup>, AND VICTOR M. CALO<sup>★</sup>

ABSTRACT. Flow liquefaction remains one of the most critical threats to the stability of Tailings Storage Facilities (TSFs), and its reliable prediction has long been hindered by a fundamental numerical pathology: mesh-dependent localization in computational models. This study demonstrates that fully coupled hydro-mechanical formulations overcome this limitation by embedding pore-pressure diffusion directly into the governing equations, thereby introducing a physically consistent internal length scale absent in uncoupled or purely mechanical approaches. Our spectral analysis yields a dispersion relation governing the growth of perturbations in the coupled system. Stability emerges when short-wave modes are sufficiently damped—a condition that requires time-step increments to exceed a critical threshold. The resulting diffuse localization bandwidth is not arbitrary but scales systematically with material and loading parameters: permeability, fluid and skeleton compressibility, and the time-step increment, expressed as a function of the load increment and its rate of application. Thus, the coupled formulation transforms an ill-posed mesh-dependent problem into a well-regularized one via an intrinsic diffusion length scale. Our numerical simulations span scales from axisymmetric triaxial tests to full TSF configurations and systematically validate our theoretical predictions. Large enough time steps suppress spurious mesh-aligned bands that plague uncoupled models. Reducing permeability—or increasing the skeleton’s compressibility—narrows shear zones and lowers the triggering load for localization, ultimately approaching the undrained limit. Load-rate effects follow a predictable pattern: at sufficiently high rates, the system transitions to undrained behavior regardless of permeability, as pore-pressure diffusion becomes negligible compared to loading timescales. We bridge analytical derivations, laboratory-scale validations, and engineering-scale modeling to establish that fully coupled formulations not merely as a numerical convenience but as a rigorous and predictive framework for assessing partially drained liquefaction triggers in tailings dams. We advance both the theoretical understanding of diffuse strain localization in fluid-saturated porous media and the practical reliability of safety analyses for critical infrastructure. We elucidate the physical mechanisms governing shear band formation under partially drained conditions, providing engineers with a principled basis for evaluating liquefaction susceptibility in TSFs.

4 CONTENTS

5	Key Points	2
6	1. Introduction	2
7	2. Spectral Stability Analysis of Fully Coupled Hydromechanical Systems	5
8	2.1. Governing Equations and Constitutive Framework	5
9	2.2. Normal-Mode Perturbation Analysis	7
10	2.3. Mass Balance in Fourier Space	9
11	2.4. Coupled Spectral System and Dispersion Relations	10
12	3. One-Dimensional Spectral Reduction	12
13	3.1. Simplified Dispersion Relation	12
14	3.2. Implementation Guidelines for Numerical Stability in Fully-coupled Simulations	13
15	3.3. Load Rate Effects and Shear Bandwidth Control	14
16	4. Flow-liquefaction under a fully-coupled scheme	15
17	4.1. Constitutive Model, Material Coupling, and Mesh Regularization	15
18	4.2. Triaxial Test	16
19	4.3. TSF Flow-liquefaction Analysis	18
20	4.4. Influence of Load Rate $r$ on Diffuse Localization Bandwidth	20
21	4.5. Influence of Permeability on Diffuse Localization Bandwidth	24
22	4.6. Influence of Tailings Compressibility on Diffuse Localization bandwidth	28

(‡) PRINCIPAL TAILINGS ENGINEER, MINE WASTE, WSP, PERTH, AUSTRALIA

(\*) SENIOR TAILINGS ENGINEER, MINE WASTE, WSP, ARGENTINA

(†) TAILINGS ENGINEER, MINE WASTE, WSP, PERTH, AUSTRALIA

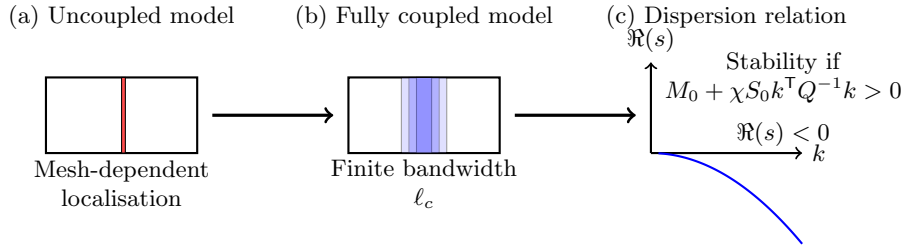
(★) DISTINGUISHED PROFESSOR, CURTIN UNIVERSITY, PERTH, AUSTRALIA

Date: April 7, 2026.

## KEY POINTS

25

- 26 (1) Fully coupled hydro-mechanical formulations suppress mesh dependency by embedding a physically consistent internal length scale through pore-pressure diffusion.
- 27
- 28 (2) An analytical equation that describes how material and numerical parameters affect the diffuse strain localization bandwidth induced by the fully coupled scheme during flow liquefaction is derived.
- 29
- 30
- 31 (3) Spectral analysis shows that stability requires short-wave modes to be damped by increments larger than a critical threshold, linking time stepping directly to diffuse localization width.
- 32
- 33 (4) Triaxial simulations confirm this prediction: when  $\Delta t$  exceeds the threshold, shear localization stabilizes into a finite-width band independent of mesh resolution.
- 34
- 35 (5) At the TSF scale, permeability, loading rate, fluid and skeleton compressibility, and increment size jointly control the onset of liquefaction and the geometry of shear bands, providing a unifying interpretation across scales.
- 36
- 37
- 38 (6) Beyond a critical load-rate threshold, the response becomes undrained and insensitive to further rate increases; below it, partially drained conditions significantly alter triggering loads.
- 39



**Graphical Abstract.** (a) In uncoupled models, localization collapses into single elements, producing mesh-dependent and non-physical results. (b) Fully coupled hydro-mechanical formulations introduce pore-pressure diffusion, which regularizes localization and enforces a finite characteristic bandwidth  $\ell_c$ . (c) The dispersion relation predicts this behavior and provides the scaling law  $\ell_c \sim \sqrt{D_{\text{eff}} \Delta t}$ , consistent with both numerical simulations and analytical derivations.

40

## 1. INTRODUCTION

41 Flow liquefaction remains one of the most critical threats to the safety of tailings storage facilities (TSFs). Even modest disturbances—sudden loads, toe displacements, phreatic surface rises, or water inflows—can trigger runaway failure if the coupled soil–fluid system becomes unstable (Ledesma et al., 2022). Numerical modeling has therefore become indispensable for vulnerability assessment. External actions are progressively applied until failure, thereby enabling quantification of safety margins (Rógenes et al., 2024). Interest in such models has intensified following post-mortem assessments of catastrophic TSF failures: Mount Polley (Morgenstern et al., 2015), Cadia (Jefferies et al., 2019), Córrego do Feijão (Brumadinho) (CIMNE/UPC, 2021), and Merriespruit (Mánica et al., 2021) among them.

49 (Jefferies and Been, 2016a) (Zienkiewicz et al., 1999; de Souza Neto et al., 2008)

50 A central challenge in these simulations is the reliable representation of strain-softening behaviour. The term *softening* is used in the geomechanics literature with two distinct meanings that require explicit clarification. In classical constitutive plasticity, softening denotes weakening of intrinsic material strength—a negative hardening modulus and contraction of the elastic domain—and is generally identified through a peak in mobilised friction (Zienkiewicz et al., 1990, 1999). In this context, softening is not necessarily associated with a decrease in deviatoric stress: an overconsolidated clay subjected to undrained shearing may exhibit a continuously increasing deviatoric stress in  $p'$ – $q$  space while still displaying a peak in mobilised friction, and therefore undergoes classical softening behaviour. In contrast, in the liquefaction and tailings engineering literature, softening is used phenomenologically to describe the stress-path-dependent reduction of undrained shear resistance driven by pore-pressure generation

51

52

53

54

55

56

57

58

59

60 and effective stress redistribution (Jefferies and Been, 2016a). This behaviour is characterised by a peak  
 61 followed by a drop in undrained resistance, which typically manifests as a reduction in deviatoric stress  
 62 or stress ratio under undrained loading, without implying any weakening of intrinsic material properties.  
 63 An important diagnostic follows: loose sands in undrained behaviour may exhibit a peak in deviatoric  
 64 stress while the mobilized friction increases monotonically; such cases do not correspond to classical con-  
 65 stitutive softening, yet they are often described as softening in the liquefaction engineering literature due  
 66 to the loss of undrained resistance driven by pore-pressure build-up. Because the present study focuses  
 67 on liquefaction triggering in tailings materials, the term softening is used in a broader phenomenological  
 68 sense. When referring specifically to this mechanism, the term *pore-pressure driven softening* is used, as  
 69 it more accurately reflects the partially-drained conditions and pore-pressure diffusion processes captured  
 70 by the fully coupled formulation.

71 Constitutive models grounded in classical plasticity theory—HSsmall (Brinkgreve et al., 2020), Nor-  
 72 Sand (Jefferies and Been, 2016b), and other critical-state frameworks—capture stiffness and post-peak  
 73 weakening effectively (F. Lopez Rivarola, 2023; Tasso et al., 2024). Yet their predictive capacity depends  
 74 critically on the surrounding numerical formulation. Purely mechanical or uncoupled flow–deformation  
 75 analyses suffer from a fundamental pathology: once ellipticity is lost at the onset of bifurcation, strains  
 76 localize into zero-thickness bands leading into a reduction of the global load-carrying capacity. The com-  
 77 puted response then reflects mesh discretization rather than material behavior, leading to non-objective  
 78 results and compromising the reliability of stability assessments (Rudnicki and Rice, 1975; Vermeer and  
 79 de Borst, 1984). This loss of uniqueness and the associated bifurcation behavior have been extensively  
 80 analyzed in the context of non-associated plasticity and geomaterial instability. (Sulem and Vardoulakis,  
 81 1995; Nova and Hueckel, 1981; Nova, 1994; Zienkiewicz et al., 1999).

82 To restore well-posedness, constitutive models must be augmented with an internal length scale that  
 83 spreads deformation over a finite width. Two broad regularization strategies prevail in geomechanics (Oka  
 84 and Kimoto, 2012). *Nonlocal or gradient regularization* replaces the local driving variable—typically  
 85 plastic strain—with an averaged or gradient-enhanced counterpart, often through a Helmholtz-type  
 86 equation. The internal length parameter then explicitly governs the shear-band thickness (Jirásek and  
 87 Bažant, 2002; Mühlhaus and Aifantis, 1991). *Viscoplastic regularization* introduces a material time scale  
 88 so that softening unfolds at finite rates, typically via Perzyna or Duvaut–Lions overstress formulations.  
 89 This rate dependence diffuses plastic strain both temporally and spatially, thereby mitigating mesh bias  
 90 (Perzyna, 1966; Duvaut and Lions, 1976). Complementary approaches include Cosserat and micropolar  
 91 continua, which embed couple stresses and rotational degrees of freedom, and energy-based (crack-band)  
 92 regularization, which enforces finite dissipation per unit area at the integration-point level (Bažant and  
 93 Oh, 1983; Mühlhaus and Aifantis, 1991). Although this pathology and its remedies are well established  
 94 in broader geomechanics (Mánica et al., 2018; Cui et al., 2023; Rødvand et al., 2023), comparatively little  
 95 attention has been devoted to mesh objectivity within tailings-dam analyses (Sottile et al., 2021; Rivarola  
 96 and Tasso, 2024). This gap is significant. Tailings often exist in loose, contractive states susceptible  
 97 to liquefaction, where accurate prediction of triggering loads and failure modes is critical for public  
 98 safety and environmental protection. From a broader porous-media perspective, strain localization and  
 99 bifurcation under hydro-mechanical coupling have been investigated in both saturated and unsaturated  
 100 conditions, highlighting the role of permeability, compressibility, and diffusion processes in controlling  
 101 instability development. (Schrefler et al., 1995; Zhang et al., 1999; Shahbodagh et al., 2023)

102 Fully coupled hydro-mechanical formulations offer an alternative path to regularization—one that  
 103 introduces no ad hoc parameters. By solving for displacement and pore pressure simultaneously, the  
 104 formulation embeds the fluid mass balance directly in the governing equations. This introduces diffusion  
 105 as an intrinsic regularization mechanism. The coupling between pore pressure and volumetric strain  
 106 causes the fluid phase to act as a buffer: it opposes rapid volumetric changes, diffusing deformation  
 107 in both time and space. Storage terms and Darcy flux together attenuate short-wavelength pertur-  
 108 bations, stabilizing the softening response and improving uniqueness (Coussy, 2003). Physically, the  
 109 diffusion length scale arises from hydraulic diffusivity—a material property governed by permeability  
 110 and compressibility—rather than from an externally imposed parameter. The same framework tran-  
 111 sitions naturally between drained, partially drained, and undrained regimes without invoking ad hoc  
 112 drainage assumptions, capturing the full spectrum of field loading conditions.

113 From a constitutive standpoint, it is important to distinguish between diffuse instability mechanisms  
 114 and localized failure modes. Diffuse constitutive instabilities have been analysed as material-point phe-  
 115 nomena that do not rely on the formation of a shear band driven by loss of ellipticity. Related concepts  
 116 of diffuse bifurcation, controllability, and incremental instability have been extensively explored within  
 117 non-associated plasticity and geomaterial mechanics (Darve et al., 2007; Darve and Laouafa, 2000; Nova,

118 1994). Our goal is to clarify how fully coupled formulations regularize pore-pressure driven softening  
 119 instabilities in loose tailings and to establish quantitative relationships between material properties,  
 120 loading conditions, and diffuse localization behavior. Diffuse constitutive instabilities are not treated  
 121 as localization criteria at the material-point level, but rather as the underlying mechanism that, when  
 122 embedded in a fully coupled hydro-mechanical boundary-value problem, governs the spatial redistribu-  
 123 tion of deformation and pore pressure under nearly undrained loading conditions. Using spectral  
 124 analysis in Fourier–Laplace space, we derive a dispersion relation that governs perturbation growth in  
 125 the linearized system. In this sense, this proposal results in an extension of earlier acoustic tensor-based  
 126 analyses (Rudnicki and Rice, 1975), where the hydro-mechanical coupling naturally introduces character-  
 127 istic time- and length-scales absent in purely mechanical treatments. Finally, the analysis identifies the  
 128 parameters controlling the diffuse finite localization bandwidth: hydraulic diffusivity (permeability and  
 129 fluid/skeleton compressibility), loading rate, and constitutive softening rate. Short-wavelength modes  
 130 are damped when time increments exceed a critical threshold, ensuring that shear bands possess finite,  
 131 mesh-independent width.

132 Related dispersion-based analyses of strain localization in fluid-saturated porous media have been  
 133 previously reported, where internal length scales emerge from coupled solid–fluid interactions (Schrefler  
 134 et al., 1995; Zhang et al., 1999). Those studies primarily address dynamic or wave-propagation regimes  
 135 and interpret localization through dispersion relations associated with constitutive softening and loss  
 136 of hyperbolicity. By contrast, the present work focuses on quasi-static, fully coupled boundary-value  
 137 problems relevant to liquefaction triggering, in which the characteristic length scale arises from pore-  
 138 pressure diffusion and loading-rate effects, rather than from wave-dispersion mechanisms.

139 We validate our analytical predictions with numerical simulations performed in PLAXIS 2D using the  
 140 HSsmall constitutive model and a van Genuchten soil-water retention curve. The adoption of the HSsmall  
 141 and van Genuchten models reflects a pragmatic modelling choice widely used by tailings practitioners  
 142 in industry and academia, aimed at ensuring a robust and consistent fully coupled formulation under  
 143 drained, partially drained, and undrained conditions. The limitations associated with this constitutive  
 144 choice are explicitly discussed later in the manuscript.

145 Simulations span two scales: axisymmetric triaxial tests that isolate fundamental mechanisms under  
 146 controlled boundary conditions, and TSF-scale scenarios that incorporate realistic geometries, load-  
 147 ing sequences, and heterogeneities. Triaxial tests reveal how time increment selection influences the  
 148 emergence of short-wavelength noise in shear-band contours—a signature of inadequate regularization.  
 149 TSF-scale liquefaction-triggering exercises demonstrate how external load rate, permeability, and skele-  
 150 ton compressibility collectively determine shear-band width and the critical load required to initiate  
 151 flow liquefaction. As permeability decreases or skeleton compressibility increases, the system transitions  
 152 progressively toward undrained conditions: shear bands narrow, triggering loads decrease, and mesh  
 153 dependence vanishes. Load-rate effects are predictable: high loading rates suppress drainage and induce  
 154 an undrained response regardless of permeability. By linking analytical conditions to numerical evidence  
 155 across scales, we establish a consistent framework connecting laboratory observations, computational  
 156 modeling, and field-scale liquefaction behavior. This framework provides engineers with a principled  
 157 basis for selecting time increments, interpreting shear-band formation, and assessing liquefaction suscep-  
 158 tibility in partially drained tailings without relying on nonphysical regularization parameters.

159 This paper is organized as follows. Section 2 summarizes the governing equations of fully cou-  
 160 pled poroelastoplasticity, linearizes them about a critical state, and derives the dispersion relation in  
 161 Fourier–Laplace space for a general multidimensional setting. Section 3 reduces the equations to one  
 162 spatial dimension, extracting practical guidelines for fully coupled simulations and providing an esti-  
 163 mate of the induced shear-band width that underpins mesh-independent results in partially drained and  
 164 undrained regimes. Section 4 presents numerical validation: triaxial-test simulations demonstrate the  
 165 role of time increments in suppressing spurious short-wavelength modes, while TSF-scale liquefaction-  
 166 triggering exercises reveal how load rate, permeability, and skeleton compressibility govern shear-band  
 167 evolution and failure initiation. Finally, Section 5 synthesizes findings and discusses implications for  
 168 current TSF design and stability assessment practice.

## 169 2. SPECTRAL STABILITY ANALYSIS OF FULLY COUPLED HYDROMECHANICAL SYSTEMS

170 The spectral analysis of fully coupled hydromechanical systems reveals the fundamental mechanisms  
 171 by which pore pressure diffusion stabilizes material response and interacts with pore-pressure driven  
 172 strain-softening behavior. We linearize about a homogeneous reference state and perform a normal-  
 173 mode perturbation analysis, deriving dispersion relations that explain why localization manifests with a  
 174 finite bandwidth rather than collapsing into arbitrarily thin shear bands. This spectral analysis guides

175 our numerical implementation, particularly for selecting stable time steps and load increments in coupled  
176 simulations.

177 **2.1. Governing Equations and Constitutive Framework.** We begin by recalling the governing  
178 equations for fully coupled flow–deformation problems, in which the displacement field  $\mathbf{u}$  and the pore  
179 water pressure  $p$  serve as the primary unknowns. The framework adopted here follows the general  
180 hydromechanical formulation described in the PLAXIS manual (Brinkgreve et al., 2020), but simplified  
181 to exclude thermal effects.

182 The coupled hydromechanical system begins with fundamental kinematic and stress decomposition.  
183 The symmetric strain tensor  $\boldsymbol{\varepsilon}(\mathbf{u})$  captures deformation kinematics:

$$(1) \quad \boldsymbol{\varepsilon}(\mathbf{u}) = \frac{1}{2} (\nabla \mathbf{u} + \nabla^T \mathbf{u}), \quad \varepsilon_v = \text{tr } \boldsymbol{\varepsilon}(\mathbf{u}),$$

184 where  $\nabla$  is the spatial gradient, the superscript  $T$  implies transpose. The trace operator  $\text{tr}$  sums the  
185 diagonal entries of the tensor  $\boldsymbol{\varepsilon}(\mathbf{u})$  (i.e.,  $\text{tr } \boldsymbol{\varepsilon} = \varepsilon_{ii}$ , where repeated indexes imply summation over the  
186 index range). The total stress  $\boldsymbol{\sigma}$  decomposes into effective stress  $\boldsymbol{\sigma}'$  and pore pressure  $p$  contributions:

$$(2) \quad \boldsymbol{\sigma} = \boldsymbol{\sigma}' + \chi p \mathbf{I}.$$

187 Here  $\chi$  represents Biot’s coefficient, linking solid skeleton deformation to pore pressure,  $\varepsilon_v$  denotes the  
188 volumetric strain, and  $\mathbf{I}$  the identity tensor.

189 The governing equations for the quasi-static coupled system comprise two fundamental balances and  
190 a flow equation:

$$(3) \quad \nabla \cdot \boldsymbol{\sigma} = -\rho \mathbf{g} \quad (\text{Momentum balance})$$

$$(4) \quad M(p) \dot{p} - S(p) \dot{\varepsilon}_v = \nabla \cdot \mathbf{J}_w \quad (\text{Mass balance})$$

$$(5) \quad \mathbf{J}_w = \mathbf{C}_w(S) (\nabla p + \rho_w \mathbf{g}) \quad (\text{Darcy flow})$$

191 where the storage coefficient becomes

$$(6) \quad M(p) = n \left( S(p) \alpha_{wP} - \frac{\partial S}{\partial p}(p) \right),$$

192 and the hydraulic conductivity tensor is

$$(7) \quad \mathbf{C}_w(S) = \frac{k^{\text{rel}}(S)}{\mu} \mathbf{K}_{\text{sat}}.$$

193 Here, the porosity is  $n$ , the pressure-dependent degree of saturation is  $S(p)$ , and the mixture density  
194 is  $\rho = (1 - n)\rho_s + nS\rho_w$ , with  $\rho_s$  and  $\rho_w$  the solid and fluid densities, respectively. Moreover, the water  
195 compressibility is denoted  $\alpha_{wP}$ , while the fluid flux  $\mathbf{J}_w$  follows the Darcy law,  $\mathbf{K}^{\text{sat}}$  is the saturated  
196 permeability tensor,  $k^{\text{rel}}(S)$  is the relative permeability derived from the Soil–Water Characteristic Curve  
197 (SWCC), and  $\mu$  is the pore–fluid viscosity. Equation (3) expresses the balance of linear momentum in the  
198 porous skeleton, including pore pressure contributions, while (4) enforces mass conservation of the fluid  
199 phase. In the special case of full saturation ( $S = 1$ ) and nearly constant compressibility, (4) simplifies to  
200 a consolidation-type equation. Coupled with (3), this recovers Terzaghi’s one-dimensional consolidation  
201 theory as a limiting case. The fully coupled system collapses to a purely mechanical formulation under  
202 two extreme assumptions: (i) undrained conditions or (ii) drained conditions. Undrained conditions arise  
203 when permeability is negligible or when loading is extremely rapid, preventing the dissipation of excess  
204 pore pressures. Drained conditions occur when permeability is effectively infinite, or loading is very slow,  
205 allowing instantaneous pore–pressure equilibration. In these limits,  $\mathbf{J}_w \approx \mathbf{0}$  or  $\partial p / \partial t \approx 0$ , and the mass  
206 balance, (4), ceases to influence the mechanical response. Thus, the remaining momentum balance, (3),  
207 governs the response, with the pore pressure  $p$  interpreted either as a constant undrained pressure field  
208 or discarded entirely in dry or drained conditions. This reduction aligns with deformation-only analyses  
209 common in engineering practice. *Yet it is precisely in such simplified settings that pathological mesh*  
210 *sensitivity emerges under pore–pressure driven strain–softening conditions.* The coupling term in (4)  
211 introduces the storage coefficient  $M(p)$ , which encodes how pore pressure changes affect both fluid  
212 compressibility and saturation-dependent storage capacity.

213 In addition, this mass-balance equation adds a subtle but decisive effect: an effective viscous-like  
214 resistance that regularizes the mechanical problem. This viscous-like character arises from the dissipative  
215 drag between the solid skeleton and the pore fluid introduced by the Darcy flux, and has a physical role  
216 that differs from viscosity in fluid mechanics; it should therefore be interpreted as a phenomenological  
217 rather than a mechanical analogy. Because pore pressure and volumetric strain evolve coupled, the fluid  
218 phase acts as a buffer against abrupt volumetric changes, diffusing deformation in both time and space.

219 This mechanism delays localization and enforces a finite bandwidth for deformation zones, with physical  
 220 dissipation provided by the Darcy term, while the storage coefficient governs the capacity and rate of  
 221 pore-pressure evolution, suppressing short-wavelength perturbations that would otherwise concentrate  
 222 deformation into vanishingly thin shear bands.

223 Previous theoretical studies have demonstrated that the introduction of an additional diffusion equa-  
 224 tion restores uniqueness in the evolution of the plastic multiplier in coupled geomechanical problems  
 225 including inertia effects, thereby regularizing the overall solution (Schrefler et al., 1995; Zhang et al.,  
 226 1999; Coussy, 2003). The strength of this regularization, however, depends critically on both material  
 227 parameters—such as permeability, compressibility, and SWCC characteristics—and numerical aspects,  
 228 including the chosen time-stepping scheme. Identifying which factors dominate, and how they govern  
 229 the emergent width of localization zones, remains a central question. Addressing this interplay between  
 230 material physics and numerical resolution is the focus of this paper.

231 **Elastoplastic Constitutive Response.** The effective stress evolves according to elastoplastic theory.  
 232 In rate form, the constitutive response reads:

$$(8) \quad \dot{\boldsymbol{\sigma}}' = \mathbf{C}^e : \dot{\boldsymbol{\varepsilon}} - \lambda \mathbf{C}^e : \mathbf{M},$$

233 where  $\mathbf{C}^e$  denotes the elastic moduli (stiffness) tensor,  $\lambda \geq 0$  is the plastic multiplier, and  $\mathbf{M} = \partial G / \partial \boldsymbol{\sigma}$   
 234 represents the plastic flow direction derived from potential  $G(\boldsymbol{\sigma})$ .

235 Plastic admissibility requires stress states to satisfy  $F(\boldsymbol{\sigma}, \kappa) \leq 0$ , where  $F$  is the yield function and  
 236  $\kappa$  represents internal hardening variables. During plastic loading, the consistency condition  $\dot{F} = 0$   
 237 determines the plastic multiplier through:

$$(9) \quad \lambda = \frac{\mathbf{N} : \mathbf{C}^e : \dot{\boldsymbol{\varepsilon}}}{H + \mathbf{N} : \mathbf{C}^e : \mathbf{M}},$$

238 where  $\mathbf{N} = \partial F / \partial \boldsymbol{\sigma}$  is the yield surface normal and  $H = \partial F / \partial \kappa$  governs the effective hardening ( $H > 0$ ) or  
 239 effective softening ( $H < 0$ ) behavior. This framework naturally accommodates both associative plasticity  
 240 ( $F = G$ ) and non-associative flow ( $F \neq G$ ).

241 **Linearization and Incremental Tangent Operators.** We perform the spectral analysis by first  
 242 linearizing the governing equations around a homogeneous reference state  $(\mathbf{u}_0, p_0)$  characterized by rates  
 243  $(\dot{p}_0, \dot{\varepsilon}_{v0}, \nabla p_0)$ . We then introduce the incremental perturbations  $(\delta \mathbf{u}, \delta p)$  that represent Newton directions  
 244 or modal perturbations. Thus, the elastoplastic tangent modulus becomes:

$$(10) \quad \mathbf{C}^{ep} = \left. \frac{\partial \boldsymbol{\sigma}'}{\partial \boldsymbol{\varepsilon}} \right|_0 = \mathbf{C}^e - \frac{\mathbf{C}^e : \mathbf{M} \otimes \mathbf{N} : \mathbf{C}^e}{H + \mathbf{N} : \mathbf{C}^e : \mathbf{M}},$$

245 while hydraulic properties linearize as:

$$(11) \quad M_0 = M(p_0), \quad S_0 = S(p_0), \quad M_p = \left. \frac{dM}{dp} \right|_{p_0}, \quad S_p = \left. \frac{dS}{dp} \right|_{p_0},$$

$$(12) \quad \mathbf{C}_{w0} = \mathbf{C}_w(S_0), \quad \mathbf{C}'_w = \left. \frac{d\mathbf{C}_w}{dS} \right|_{S_0} = \frac{1}{\mu} \mathbf{K}_{\text{sat}} \left. \frac{dk_{\text{rel}}}{dS} \right|_{S_0}.$$

246 The linearized momentum balance becomes:

$$(13) \quad \nabla \cdot (\mathbf{C}^{ep} : \boldsymbol{\varepsilon}(\delta \mathbf{u})) + \chi \delta p \mathbb{I} = \mathbf{0},$$

247 and the linearized mass balance yields:

$$(14) \quad M_0 \delta \dot{p} + M_p \dot{p}_0 \delta p - S_0 \delta \dot{\varepsilon}_v - S_p \dot{\varepsilon}_{v0} \delta p \\ - \nabla \cdot (\mathbf{C}_{w0} \nabla \delta p) - \nabla \cdot (\mathbf{C}'_w S_p \delta p (\nabla p_0 + \rho_w \mathbf{g})) = 0.$$

248 **Physical Interpretation and Coupling Mechanisms.** The linearized (incremental) momentum  
 249 equation (13) highlights the interplay between mechanical and hydraulic perturbations. Mechanical  
 250 disturbances propagate through the elastoplastic stiffness tensor  $\mathbf{C}^{ep}$ , while pore-pressure fluctuations  
 251 couple to deformation via Biot's coefficient  $\chi$ . When the hardening modulus  $H < 0$ , the material ex-  
 252 hibits *effective strain-softening* (also referred to as frictional softening), which can destabilize the tangent  
 253 stiffness and promote localization. Alternatively, *flow* or *static liquefaction* may occur when the plastic  
 254 flow potential has a negative derivative with respect to the first stress invariant—indicating a contrac-  
 255 tive material response. The mass incremental balance equation (14) governs how pore pressure evolves  
 256 under these conditions. The terms  $M_0 \delta \dot{p}$  and  $S_0 \delta \dot{\varepsilon}_v$  represent fluid storage and volumetric coupling  
 257 between the solid skeleton and the pore fluid. The diffusion term,  $\nabla \cdot (\mathbf{C}_{w0} \nabla \delta p)$ , introduces a stabili-  
 258 zing mechanism: it redistributes pressure gradients in space and time, mitigating abrupt volumetric

259 changes and delaying the onset of diffuse localization. The additional terms involving  $M_p$ ,  $S_p$ , and  $\mathbf{C}'_w$   
 260 capture nonlinear contributions from pressure-dependent storage and saturation-controlled permeability,  
 261 which become increasingly relevant under partially drained or unsaturated conditions. Together, these  
 262 terms define the coupled dynamics that govern the initiation, growth, and eventual stabilization of pore-  
 263 pressure driven strain-softening instabilities in saturated geomaterials. Thus, this linearized framework  
 264 underpins spectral analysis, revealing how diffusion length scales compete with mechanical instability  
 265 wavelengths to determine the characteristic size of localization phenomena. The interplay between these  
 266 mechanisms governs whether systems exhibit diffuse deformation, sharp localization, or intermediate  
 267 band-like structures.

268 **Implications for Numerical Implementation.** The spectral structure embedded in equations (13)-  
 269 (14) guides our discussion. The coupling between mechanical and hydraulic time scales requires careful  
 270 consideration of temporal discretization schemes. The diffusion-dominated terms impose explicit time-  
 271 stepping limitations, whereas the mechanical coupling may require implicit treatment of certain terms.  
 272 Furthermore, the wavelength selection inherent in the spectral analysis provides natural guidelines for  
 273 the spatial discretization. Elements much smaller than the characteristic diffusion length fail to capture  
 274 the physics properly, while elements much larger miss essential localization features. Thus, this spectral  
 275 perspective bridges theoretical understanding with practical computational requirements, ensuring that  
 276 numerical simulations capture the essential physics of coupled hydromechanical systems.

277 **2.2. Normal-Mode Perturbation Analysis.** We investigate the spectral properties of the linearized  
 278 system in Section 2.1 by introducing normal-mode perturbations that capture both spatial and temporal  
 279 variations. This approach transforms the partial differential equations into algebraic eigenvalue problems,  
 280 revealing the fundamental wavelengths and growth rates that govern the system's stability. The analysis  
 281 is restricted to quasi-static hydromechanical conditions formulated in a standard displacement-pressure  
 282  $u$ - $p$  framework, where inertia effects are neglected; extensions to displacement-velocity-pressure  $u$ - $U$ - $p$   
 283 formulations, in which solid and fluid inertia introduce wave-propagation mechanisms and additional  
 284 characteristic scales, are beyond the scope of the present study.

285 **Fourier-Laplace Transform of Perturbations.** We introduce perturbations of Fourier-Laplace type  
 286 around the homogeneous reference state (Gerolymatou et al., 2024)

$$(15) \quad \{\delta \mathbf{u}, \delta p\} = \{\hat{\mathbf{u}}, \hat{p}\} e^{i\mathbf{k} \cdot \mathbf{x} + st},$$

287 where  $\mathbf{k} \in \mathbb{R}^3$  represents the wave vector with magnitude  $k = \|\mathbf{k}\|$ , and  $s \in \mathfrak{C}$  denotes the complex  
 288 growth rate. Let  $i^2 = -1$ . The real part  $\Re(s)$  determines the stability of the problem solution: positive  
 289 values indicate exponential growth leading to instability, while negative values correspond to decay. The  
 290 imaginary part  $\Im(s)$  governs oscillatory behavior, revealing the natural frequencies of the coupled system.

291 This normal-mode ansatz effectively decomposes the infinite-dimensional dynamical system into a  
 292 discrete spectrum of modes, each characterized by its wavelength  $\lambda = 2\pi/k$  and growth rate  $s$ . The  
 293 physical interpretation is that short wavelengths (large  $k$ ) correspond to highly localized perturbations,  
 294 whereas long wavelengths correspond to more diffuse deformation patterns.

295 **Transformation of the Momentum Balance.** We first evaluate spatial derivatives to substitute the  
 296 normal-mode ansatz (15) into the linearized momentum balance (13). Thus, the strain tensor for the  
 297 perturbation becomes:

$$(16) \quad \boldsymbol{\varepsilon}(\delta \mathbf{u}) = \frac{i}{2} (\mathbf{k} \otimes \hat{\mathbf{u}} + \hat{\mathbf{u}} \otimes \mathbf{k}) e^{i\mathbf{k} \cdot \mathbf{x} + st},$$

298 where the factor  $i$  arises from spatial differentiation and the tensor product captures the symmetric  
 299 nature of the strain.

300 The divergence of the effective stress contribution requires detailed analysis. Using index notation  
 301 with the Einstein summation convention, we have:

$$(17) \quad \varepsilon_{pq}(\delta \mathbf{u}) = \frac{1}{2} (\partial_p \delta u_q + \partial_q \delta u_p) = \frac{i}{2} (k_p \hat{u}_q + k_q \hat{u}_p) e^{i\mathbf{k} \cdot \mathbf{x} + st},$$

$$(18) \quad \sigma'_{mn} = C_{mnpq}^{ep} \varepsilon_{pq}(\delta \mathbf{u}) = C_{mnpq}^{ep} \frac{i}{2} (k_p \hat{u}_q + k_q \hat{u}_p) e^{i\mathbf{k} \cdot \mathbf{x} + st}.$$

302 Taking the divergence and exploiting the minor symmetry  $C_{mnpq}^{ep} = C_{mnpq}^{ep}$ , which cancels the factor  
303 of 1/2, yields:

$$(19) \quad \begin{aligned} [\nabla \cdot (\mathbb{C}^{ep} : \boldsymbol{\varepsilon}(\delta \mathbf{u}))]_n &= \partial_m \sigma'_{mn} = ik_m C_{mnpq}^{ep} \frac{i}{2} (k_p \hat{u}_q + k_q \hat{u}_p) e^{i\mathbf{k} \cdot \mathbf{x} + st} \\ &= -C_{mnpq}^{ep} k_m k_p \hat{u}_q e^{i\mathbf{k} \cdot \mathbf{x} + st}, \end{aligned}$$

304 where we used  $i^2 = -1$  and the symmetry property.

305 The pressure gradient term transforms more straightforwardly:

$$(20) \quad \nabla \cdot (\chi \delta p \mathbf{I}) = \chi \nabla \delta p = i\chi \mathbf{k} \hat{p} e^{i\mathbf{k} \cdot \mathbf{x} + st}.$$

306 **The Acoustic Tensor and Reduced Momentum Equation.** Combining equations (19) and (20),  
307 the linearized momentum balance reduces to:

$$(21) \quad -C_{mnpq}^{ep} k_m k_p \hat{u}_q + i\chi k_n \hat{p} = 0.$$

308 since the common exponential factor is non-zero for all combinations of  $\mathbf{k}$  &  $\mathbf{x}$  and  $s$  &  $t$ .

309 We express this algebraic equation compactly by introducing the *acoustic tensor*:

$$(22) \quad Q_{nq}(\mathbf{k}) := C_{mnpq}^{ep} k_m k_p,$$

310 which encapsulates the material's directional stiffness properties along the wave-vector direction. The  
311 momentum balance then becomes:

$$(23) \quad \mathbf{Q}(\mathbf{k}) \hat{\mathbf{u}} - i\chi \mathbf{k} \hat{p} = \mathbf{0}.$$

312 **Coupling Structure and System Implications.** The reduced momentum balance (23) reveals the  
313 fundamental coupling between mechanical deformation and pore pressure in the spectral domain. The  
314 term  $i\chi \mathbf{k} \hat{p}$  represents how pressure gradients generate body forces that drive displacement perturba-  
315 tions. This coupling term is purely imaginary, indicating a  $90^\circ$  phase shift between pressure gradients  
316 and displacement responses. The acoustic tensor  $\mathbf{Q}(\mathbf{k})$  determines the mechanical stiffness in each wave  
317 direction, while the coupling coefficient  $\chi$  controls how strongly pressure variations influence the mechan-  
318 ical response. In the limit  $\chi \rightarrow 0$  (dry conditions), the momentum balance decouples from the pressure,  
319 reducing to the purely mechanical eigenvalue problem  $\mathbf{Q}(\mathbf{k}) \hat{\mathbf{u}} = \mathbf{0}$ .

320 This spectral representation underpins the analysis of the complete coupled system, in which the  
321 momentum equation (23) must be solved simultaneously with the transformed mass balance to determine  
322 the full spectrum of growth rates and corresponding eigenmodes.

323 **Physical and Mathematical Properties of the Acoustic Tensor.** The acoustic tensor  $\mathbf{Q}(\mathbf{k})$  inherits  
324 mechanical properties from the elastoplastic tangent modulus  $\mathbb{C}^{ep}$ . Writing  $\mathbf{k} = k\mathbf{n}$  where  $\mathbf{n}$  is the unit  
325 wave direction, we obtain:

$$(24) \quad \mathbf{Q}(\mathbf{k}) = k^2 (\mathbf{n} \cdot \mathbb{C}^{ep} \cdot \mathbf{n}),$$

326 revealing that the acoustic tensor scales quadratically with wavenumber and depends on the directional  
327 stiffness along  $\mathbf{n}$ . For stable materials (elastic and hardening),  $\mathbf{Q}(\mathbf{k})$  remains positive definite for all  $\mathbf{k} \neq \mathbf{0}$ .  
328 However, during strain-softening (frictional and pore-pressure driven softening), certain components  
329 of  $\mathbb{C}^{ep}$  may become negative, potentially rendering  $\mathbf{Q}(\mathbf{k})$  indefinite for specific wave directions. This  
330 loss of positive definiteness signals the onset of localization instabilities. Therefore, the determinant  
331  $\det[\mathbf{Q}(\mathbf{k})]$  is a scalar measure of directional stability. When this determinant vanishes for some  $\mathbf{k} \neq$   
332  $\mathbf{0}$ , the corresponding wave direction becomes neutrally stable, marking the threshold for localization.  
333 The eigenvectors of  $\mathbf{Q}(\mathbf{k})$  at this threshold define the preferred orientation of emerging localization  
334 bands (Rudnicki and Rice, 1975).

335 **2.3. Mass Balance in Fourier Space.** The transformation of the linearized mass-balance equation  
336 into Fourier space reveals the intricate interplay among diffusive stabilization, reactive coupling, and  
337 advective transport that governs the dynamics of pressure perturbations. Our analysis elucidates the  
338 contributions of various physical mechanisms to the spectral response and determines the characteristic  
339 time and length scales of the coupled system.

340 **Fourier Transformation of Mass Balance Terms.** Substituting the normal-mode ansatz (15) into  
 341 the linearized mass balance (14) and canceling the common exponential factor  $e^{i\mathbf{k}\cdot\mathbf{x}+st}$  yields:

$$(25) \quad (M_0s + M_p\dot{p}_0 - S_p\dot{\epsilon}_{v0} + \mathbf{k} \cdot \mathbf{C}_{w0} \cdot \mathbf{k} - iS_p \mathbf{k} \cdot \mathbf{C}'_w (\nabla p_0 + \rho_w \mathbf{g})) \hat{p} - S_0 s i\mathbf{k} \cdot \hat{\mathbf{u}} = 0.$$

342 This expression captures the complete spectral structure of the mass balance, encoding multiple phys-  
 343 ical processes within a single algebraic constraint. Each term carries distinct physical significance and  
 344 contributes differently to the system's overall response.

345 **Operator Decomposition and Physical Interpretation.** We elucidate the underlying physics by  
 346 decomposing the mass-balance operator into physically meaningful components. The perturbed mass  
 347 balance assumes the compact form:

$$(26) \quad A(\mathbf{k}, s)\hat{p} + B(s)i\mathbf{k} \cdot \hat{\mathbf{u}} = 0,$$

348 where the pressure operator decomposes into reactive, diffusion, and phase-drift terms:

$$(27) \quad A(\mathbf{k}, s) = A_{\text{react}}(s) + A_{\text{diff}}(\mathbf{k}) - iA_{\text{phase}}(\mathbf{k}),$$

349 and the hydromechanical coupling term is:

$$(28) \quad B(s) = -S_0s.$$

350 Each term represents a distinct physical mechanism governing the system's spectral response.

351 **Reactive Contributions.** The reactive term captures time-dependent storage and source effects:

$$(29) \quad A_{\text{react}}(s) = M_0s + \Pi_0, \quad \Pi_0 = M_p\dot{p}_0 - S_p\dot{\epsilon}_{v0}.$$

352 Here,  $M_0s$  represents the fundamental storage response proportional to the growth rate, while  $\Pi_0$  encodes  
 353 the nonlinear coupling effects arising from the background loading history. The parameter  $\Pi_0$  reflects  
 354 how pressure-dependent storage ( $M_p\dot{p}_0$ ) competes with saturation-induced storage changes ( $S_p\dot{\epsilon}_{v0}$ ) at  
 355 the reference state. This competition can either stabilize or destabilize perturbations depending on the  
 356 loading path and material properties.

357 **Diffusive Stabilization.** The diffusion term provides the primary stabilizing mechanism:

$$(30) \quad A_{\text{diff}}(\mathbf{k}) = \mathbf{k} \cdot \mathbf{C}_{w0} \cdot \mathbf{k}.$$

358 This term encodes a quadratic dependence on wave number, reflecting the second-order nature of the  
 359 diffusion operator. Short-wavelength perturbations (large  $k$ ) experience strong diffusive damping, while  
 360 long-wavelength modes remain relatively unaffected by pressure redistribution. The hydraulic conduc-  
 361 tivity tensor  $\mathbf{C}_{w0}$  determines the anisotropy and magnitude of this stabilization process, thereby directly  
 362 linking material permeability to overall system stability.

363 **Phase-Drift Effects.** The phase-drift term introduces complexity through advective transport:

$$(31) \quad A_{\text{phase}}(\mathbf{k}) = S_p \mathbf{k} \cdot \mathbf{C}'_w (\nabla p_0 + \rho_w \mathbf{g}).$$

This term arises from the nonlinear dependence of hydraulic conductivity on saturation and couples the  
 background pressure gradient to the dynamics of perturbations. The factor

$$\mathbf{C}'_w = \frac{d\mathbf{C}_w}{dS}$$

364 quantifies how permeability changes with saturation, while the vector  $(\nabla p_0 + \rho_w \mathbf{g})$  represents the de-  
 365 viation from hydrostatic equilibrium. Under hydrostatic conditions where  $\nabla p_0 + \rho_w \mathbf{g} = \mathbf{0}$ , this term  
 366 vanishes completely, reducing the operator to purely real and diffusive. However, when pressure gradi-  
 367 ents deviate from hydrostatic balance—as occurs during loading or in the presence of external forces—the  
 368 phase-drift term introduces imaginary contributions that can shift the frequencies of oscillatory modes  
 369 and potentially destabilize the system via resonance.

370 **Hydromechanical Coupling.** The coupling term (28) (i.e.,  $B(s) = -S_0s$ ) links pressure perturba-  
 371 tions to volumetric strain rates through the saturation-dependent storage coefficient  $S_0$ , a fundamental  
 372 coupling to poromechanics reflecting how skeletal deformation drives changes in pore pressure. The neg-  
 373 ative sign indicates that volumetric expansion (positive  $\mathbf{k} \cdot \hat{\mathbf{u}}$ ) reduces the pore pressure, consistent with  
 374 physical expectations. The frequency dependence of  $B(s)$  reveals that this coupling strengthens with  
 375 increasing growth rate, making high-frequency modes more susceptible to hydromechanical interaction.  
 376 Consequently, this frequency-dependent coupling gives rise to the rich spectral structure observed in  
 377 coupled poroelastic systems.

378 **2.4. Coupled Spectral System and Dispersion Relations.** The complete spectral analysis is ob-  
 379 tained by combining the transformed momentum and mass-balance equations into a unified block system.  
 380 This coupling reveals the fundamental dispersion characteristics that govern wave propagation, instability  
 381 growth, and the transition between stable and unstable regimes in saturated geomaterials.

382 **Block Matrix Formulation.** Combining equations (23) and (26), the coupled spectral system assumes  
 383 the block matrix form:

$$(32) \quad \begin{bmatrix} \mathbf{Q}(\mathbf{k}) & -i\chi\mathbf{k} \\ iB(s)\mathbf{k}^\top & A(\mathbf{k}, s) \end{bmatrix} \begin{bmatrix} \hat{\mathbf{u}} \\ \hat{p} \end{bmatrix} = \mathbf{0}.$$

384 This matrix structure encapsulates the hydromechanical coupling. The diagonal blocks represent the  
 385 individual mechanical ( $\mathbf{Q}(\mathbf{k})$ ) and hydraulic ( $A(\mathbf{k}, s)$ ) responses, while the off-diagonal terms encode the  
 386 bidirectional coupling through Biot's coefficient  $\chi$  and the storage-dependent term  $B(s)$ .

387 **Remark 1.** *The block structure reveals fundamental asymmetries in the coupling mechanism. The*  
 388 *mechanical-to-hydraulic coupling (upper-right block) depends only on the wave vector  $\mathbf{k}$ , reflecting the*  
 389 *instantaneous effect of volumetric strain on pore pressure. In contrast, the hydraulic-to-mechanical cou-*  
 390 *pling (lower-left block) involves the growth rate  $s$ , indicating that pressure-induced mechanical responses*  
 391 *depend on the time scale of the perturbation that triggers the coupling.*

392 **Remark 2.** *It is worth noting that Eq. (32) can be interpreted as an extension of the classical Rice-*  
 393 *Rudnicki (Rudnicki and Rice, 1975) bifurcation framework to fully coupled hydro-mechanical problems.*  
 394 *Block-structured dispersion relations involving both mechanical and hydraulic fields, although derived un-*  
 395 *der different assumptions, have been previously proposed in the context of poromechanical bifurcation and*  
 396 *diffuse instability analyses (Schrefler et al., 1995; Zhang et al., 1999). In contrast to purely mechanical*  
 397 *formulations, these approaches—and the present one—lead to complex-valued spectral problems in which*  
 398 *stability, diffusion, and wave propagation are intrinsically coupled.*

399 **Dispersion Relation Derivation.** Nontrivial solutions to the homogeneous system (32) require the  
 400 determinant to vanish:

$$(33) \quad \det \begin{bmatrix} \mathbf{Q}(\mathbf{k}) & -i\chi\mathbf{k} \\ iB(s)\mathbf{k}^\top & A(\mathbf{k}, s) \end{bmatrix} = 0.$$

401 Expanding this determinant using the block structure, we obtain:

$$(34) \quad A(\mathbf{k}, s) \det(\mathbf{Q}(\mathbf{k})) - \chi B(s) \mathbf{k}^\top \mathbf{Q}^{-1}(\mathbf{k}) \mathbf{k} \det(\mathbf{Q}(\mathbf{k})) = 0.$$

402 Assuming the acoustic tensor remains invertible (i.e.,  $\det(\mathbf{Q}(\mathbf{k})) \neq 0$ ), we can divide through and rear-  
 403 range terms using the definitions from (26). Substituting the expressions for  $A(\mathbf{k}, s)$  and  $B(s)$ , yields:

$$(35) \quad [M_0 + S_0\chi\mathbf{k}^\top \mathbf{Q}^{-1}(\mathbf{k})\mathbf{k}] s + \Pi_0 + A_{\text{diff}}(\mathbf{k}) - iA_{\text{phase}}(\mathbf{k}) = 0.$$

404 Solving for the growth rate  $s$  gives the fundamental dispersion relation:

$$(36) \quad \boxed{s(\mathbf{k}) = -\frac{\Pi_0 + A_{\text{diff}}(\mathbf{k}) - iA_{\text{phase}}(\mathbf{k})}{M_0 + S_0\chi\mathbf{k}^\top \mathbf{Q}^{-1}(\mathbf{k})\mathbf{k}}}$$

405 This compact expression encodes the spectral response of the coupled hydromechanical system and serves  
 406 as a foundation for understanding stability, wave propagation, and localization phenomena.

407 **Physical Interpretation of the Dispersion Relation.** The dispersion relation (36) reveals many  
 408 physical insights. The numerator combines reactive effects ( $\Pi_0$ ), diffusive stabilization ( $A_{\text{diff}}(\mathbf{k})$ ), and  
 409 phase-drift contributions ( $A_{\text{phase}}(\mathbf{k})$ ), representing the driving forces for perturbation growth or decay.

410 The denominator introduces a modified storage coefficient:

$$(37) \quad \mathcal{D}(\mathbf{k}) = M_0 + S_0\chi\mathbf{k}^\top \mathbf{Q}^{-1}(\mathbf{k})\mathbf{k},$$

411 which governs the effective time scale of the coupled response. This modified storage combines the base-  
 412 line fluid storage  $M_0$  with a mechanical contribution proportional to the inverse of the acoustic tensor.  
 413 The mechanical contribution becomes significant when the acoustic tensor approaches a singularity, indi-  
 414 cating proximity to mechanical instability. The term  $\mathbf{k}^\top \mathbf{Q}^{-1}(\mathbf{k})\mathbf{k}$  represents the mechanical compliance  
 415 in the direction of wave propagation. Large values indicate directions where the material offers little  
 416 resistance to deformation, potentially leading to preferred orientations of localization.

417 **Stability Analysis.** The stability of the coupled system depends on the real part of the growth rate  
 418 remaining non-positive for all wave vectors. This restriction implies the following constraint:

$$(38) \quad \Re[s(\mathbf{k})] = -\frac{A_{\text{diff}}(\mathbf{k}) + \Pi_0}{M_0 + S_0 \chi \mathbf{k}^T \mathbf{Q}^{-1}(\mathbf{k}) \mathbf{k}} \leq 0 \quad \forall \mathbf{k} \neq \mathbf{0}.$$

419 Since  $A_{\text{diff}}(\mathbf{k}) = \mathbf{k} \cdot \mathbf{C}_{w0} \cdot \mathbf{k} \geq 0$  always provides stabilization, the critical factor becomes the competition  
 420 between the diffusive damping and the reactive destabilization governed by  $\Pi_0$ . The modified storage  
 421 coefficient in the denominator  $\mathcal{D}(\mathbf{k})$  determines the solution stability. This discriminant defines a storage  
 422 coefficient, allowing us to distinguish between physical and singular information propagation. When  
 423  $\mathcal{D}(\mathbf{k}) > 0$ , the system exhibits conventional behavior where diffusion stabilizes short wavelengths. How-  
 424 ever, as the acoustic tensor approaches singularity (indicating mechanical instability),  $\mathcal{D}(\mathbf{k})$  can become  
 425 negative for certain wave directions, fundamentally altering the stability landscape.

426 **Critical Wavelength and Diffuse Localization.** The dispersion relation reveals characteristic length  
 427 scales that govern diffuse localization phenomena. The competition between diffusive stabilization and  
 428 mechanical destabilization determines a critical wavelength  $\lambda_c$  below which perturbations decay and  
 429 above which they may grow. For hydrostatic background conditions where  $A_{\text{phase}}(\mathbf{k}) = 0$ , the sys-  
 430 tem exhibits purely real eigenvalues, leading to monotonic growth or decay without perturbing oscilla-  
 431 tion. When the modified storage coefficient remains positive, the transition between stable and unstable  
 432 regimes occurs when:

$$(39) \quad A_{\text{diff}}(\mathbf{k}) + \Pi_0 = 0,$$

433 defining the neutral stability curve in wavenumber space.

434 **Remark 3.** *The system's anisotropy (i.e., the anisotropy of the acoustic tensor  $\mathbf{Q}(\mathbf{k})$  and the hydraulic*  
 435 *conductivity  $\mathbf{C}_{w0}$ ) creates preferential directions for the development of instability. For example, com-*  
 436 *pounding effects occur when weak directions in the acoustic tensor (near-singular eigenvectors) align*  
 437 *with low hydraulic conductivity, producing highly localized failure modes with characteristic orientations*  
 438 *determined by the material's fabric and loading history.*

439 **Implications for Multiscale Behavior.** Short wavelengths experience strong diffusive damping and  
 440 remain stable, corresponding to grain-scale fluctuations that average out over larger volumes. Inter-  
 441 mediate wavelengths may become unstable, leading to localization phenomena such as shear bands or  
 442 compaction bands. Long wavelengths approach the limit where mechanical and hydraulic responses  
 443 decouple, with the mechanical response dominated by the acoustic tensor properties and the hydraulic  
 444 response governed by large-scale pressure gradients. This scale separation underlies the effectiveness of  
 445 continuum approaches for problems involving length scales much larger than the characteristic diffusion  
 446 length. The rich spectral structure revealed by the dispersion relation allows our analysis framework to  
 447 bridge microscale material behavior with macroscale failure patterns, providing a theoretical foundation  
 448 for understanding how localized instabilities emerge from distributed loading in saturated geomaterials  
 449 under general drainage conditions.

450 **System Response and Stability Implications.** The pressure operator decomposition (27) also offers  
 451 physical insight into the system's behavior. Stability requires that the real part of  $A(\mathbf{k}, s)$  remains positive  
 452 for all physically relevant wave numbers. The diffusive term  $A_{\text{diff}}(\mathbf{k})$  always contributes a positive real  
 453 part, providing stabilization. However, the reactive term  $A_{\text{react}}(s)$  can become negative for sufficiently  
 454 large growth rates or unfavorable background conditions, potentially triggering instability.

455 The phase-drift term introduces complex dynamics into what might otherwise be straightforward dif-  
 456 fusive behavior. When pressure gradients deviate from hydrostatic equilibrium—whether through active  
 457 loading, gravitational effects, or pre-existing stress fields—this term generates imaginary components  
 458 in the growth rate that fundamentally alter the system's spectral character. Rather than simple ex-  
 459 ponential growth or decay, perturbations can now exhibit oscillatory behavior, with frequencies that  
 460 depend directly on the magnitude and direction of the background pressure gradient. These oscillations  
 461 create resonances where mechanical instabilities can couple with hydraulic pressure waves, potentially  
 462 amplifying disturbances that would otherwise decay. The stability boundaries in the complex  $s$ -plane  
 463 no longer follow simple real-axis criteria but instead trace curved paths that depend on the loading his-  
 464 tory and material state. When phase-drift effects become significant, predicting the onset of instability  
 465 requires tracking both the growth rates of amplitude and the phase relationships between mechanical  
 466 and hydraulic perturbations. This spectral framework reveals the intricate choreography among com-  
 467 peting physical processes in both fully and partially saturated tailings. Storage mechanisms determine

468 how quickly the system can respond to perturbations. Diffusion provides the primary stabilizing force,  
 469 spreading pressure disturbances across space and time. Advective transport, captured by the phase-drift  
 470 terms, can either enhance or disrupt this stabilization depending on the flow direction relative to the  
 471 instability pattern. Hydromechanical coupling directly links these hydraulic processes to mechanical  
 472 deformation, creating feedback loops that can either dampen or amplify growing instabilities.

### 473 3. ONE-DIMENSIONAL SPECTRAL REDUCTION

474 The one-dimensional reduction can improve the understanding of the fundamental mechanisms gov-  
 475 erning coupled hydromechanical stability while eliminating geometric complexities that can obscure the  
 476 underlying physics. This reduction enables us to examine in detail the essential competition between  
 477 diffusive stabilization and pore-pressure driven softening, thereby establishing the theoretical foundation  
 478 for understanding diffuse localization in more complex geometries.

479 **3.1. Simplified Dispersion Relation.** For longitudinal perturbations along the volumetric direction  
 480 with wave vector  $\mathbf{k} = k\mathbf{e}_v$ , the three-dimensional dispersion relation (36) reduces to a scalar form. The  
 481 acoustic tensor simplifies to  $\mathbf{Q}(k\mathbf{e}_v) = k^2 E_{ep}$ , where  $E_{ep}$  represents the volumetric one-dimensional  
 482 elastoplastic tangent modulus. Within the flow-liquefaction context, we interpret the elastoplastic tan-  
 483 gent modulus as a component that defines the material's compressibility. Alternatively, the diffusion term  
 484 becomes  $A_{\text{diff}}(k) = C_{w0}k^2$ , where  $C_{w0}$  is the scalar hydraulic conductivity in the volumetric direction.  
 485 The one-dimensional dispersion relation thus takes the form:

$$(40) \quad s(k) = -\frac{\Pi_0 + C_{w0}k^2 - iS_p C'_w (\partial_x p_0 + \rho_w g_x)k}{M_0 + \chi S_0/E_{ep}},$$

486 capturing the one-dimensional spectral response, including reactive contributions ( $\Pi_0$ ), diffusive stabi-  
 487 lization ( $C_{w0}k^2$ ), phase-drift effects (the imaginary term), and the modified storage coefficient in the  
 488 denominator ( $\mathcal{D} = M_0 + \chi S_0/E_{ep}$ ).

489 **Physical Interpretation of the One-Dimensional Response.** The modified storage coefficient fun-  
 490 damentally couples the hydraulic and mechanical responses. The baseline fluid storage  $M_0$  combines with  
 491 a mechanical contribution  $\chi S_0/E_{ep}$  that depends on the elastoplastic volumetric tangent modulus. When  
 492  $E_{ep}$  becomes small (more compressible material), this mechanical contribution grows large, altering the  
 493 effective storage characteristics. The numerator structure shows how different physical mechanisms com-  
 494 pete to drive stability or instability. The diffusive term  $C_{w0}k^2$  always provides stabilization proportional  
 495 to  $k^2$ , favoring the decay of short-wavelength perturbations. The reactive term  $\Pi_0$  can either stabilize or  
 496 destabilize depending on the background loading history and material nonlinearity. The phase-drift term  
 497  $S_p C'_w (\partial_x p_0 + \rho_w g_x)k$  introduces complexity through its dependence on the deviation from hydrostatic  
 498 equilibrium. This term scales linearly with wave number, creating a different wavelength dependence  
 499 than the quadratic diffusion term and potentially leading to preferential wavelength selection.

500 **Hydrostatic Equilibrium and Pure Diffusion.** Under hydrostatic conditions where the pressure  
 501 gradient balances gravity ( $\partial_x p_0 + \rho_w g_x = 0$ ) and with no background loading effects ( $\Pi_0 = 0$ ), the  
 502 dispersion relation reduces to its simplest form:

$$(41) \quad s(k) = -\frac{C_{w0}k^2}{M_0 + \chi S_0/E_{ep}} = -\frac{C_{w0}}{\mathcal{D}}k^2 = -D_{\text{eff}}k^2,$$

503 where the effective diffusion coefficient is:  $D_{\text{eff}} = C_{w0}/\mathcal{D}$ . This reduction to pure diffusive behavior  
 504 reveals the classical parabolic character of coupled poroelastic systems under equilibrium conditions. All  
 505 perturbations decay exponentially with a rate proportional to  $k^2$ , characteristic of diffusion-dominated  
 506 processes. The effective diffusion coefficient  $D_{\text{eff}}$  encodes the complete hydromechanical coupling. Unlike  
 507 simple thermal or chemical diffusion, this coefficient depends on both hydraulic properties ( $C_{w0}$ ) and  
 508 mechanical response characteristics through the modified storage term in the denominator.

509 **Stability Analysis and Pore-Pressure Driven Strain Softening.** The stability condition requires  
 510  $\Re[s(k)] \leq 0$  for all wave numbers  $k \neq 0$ . Under hydrostatic conditions, this reduces to:

$$(42) \quad D_{\text{eff}} = \frac{C_{w0}}{\mathcal{D}} \geq 0.$$

511 Since  $C_{w0} > 0$  always, stability depends entirely on the sign of the denominator  $\mathcal{D} = M_0 + \chi S_0/E_{ep}$ .  
 512 The system remains stable as long as:

$$(43) \quad \mathcal{D} = M_0 + \frac{\chi S_0}{E_{ep}} > 0 \quad \Rightarrow \quad |E_{ep}| > \frac{\chi S_0}{M_0}.$$

513 This inequality establishes a critical threshold for volumetric compressibility, which ultimately drives  
 514 flow-liquefaction. Mild softening can be tolerated without triggering instability, provided the hydraulic  
 515 storage  $M_0$  remains sufficiently large relative to the mechanical coupling strength  $\chi S_0$ .

516 **Critical Pore-Pressure Driven Softening and Wavelength Selection.** At the stability boundary  
 517 where  $M_0 + \chi S_0/E_{ep} = 0$ , the effective diffusion coefficient becomes infinite, indicating that the parabolic  
 518 character of the governing equations breaks down. Beyond this threshold, the denominator becomes  
 519 negative, which fundamentally alters the system's response. When instabilities occur, they manifest  
 520 through finite-wavelength perturbations rather than short-wavelength modes. This wavelength selection  
 521 arises from the competition between the stabilizing diffusion term  $C_{w0}k^2$  and destabilizing contributions  
 522 from background loading or mechanical coupling. The characteristic unstable wavelength depends on the  
 523 specific form of the destabilizing terms determining the expected size of the diffuse localization phenom-  
 524 ena. Short-wavelength instabilities result in thin shear bands, whereas longer-wavelength instabilities  
 525 produce more diffuse failure zones.

526 **3.2. Implementation Guidelines for Numerical Stability in Fully-coupled Simulations.** The  
 527 spectral analysis provides direct guidance for numerical implementation of coupled hydromechanical  
 528 problems. By connecting theoretical dispersion properties to computational parameters, we establish  
 529 practical criteria for sizing time steps and load increments, thereby ensuring physically meaningful results  
 530 while maintaining numerical stability.

531 **Mesh-Scale Mode Suppression and Time Step Selection.** The finite element discretization im-  
 532 poses a natural upper bound on resolvable wave numbers, as determined by the Nyquist criterion. For  
 533 a mesh with characteristic element size  $h_{\text{elem}}$ , the largest representable wave number is:

$$(44) \quad k_{\text{max}} = \frac{\pi}{h_{\text{elem}}}.$$

534 This high-frequency mode represents the finest spatial oscillation that the discretization can capture  
 535 without aliasing. However, these mesh-scale modes often lack physical significance and can contaminate  
 536 the solution if they are allowed to persist. In hydrostatic conditions, the system exhibits pure diffu-  
 537 sive behavior with effective diffusion coefficient  $D_{\text{eff}}$ , high-frequency perturbations decay exponentially  
 538 according to:

$$(45) \quad |\hat{p}(k, t)| = |\hat{p}(k, 0)|e^{-D_{\text{eff}} k^2 t}.$$

539 The characteristic decay time for the mesh-scale mode becomes:

$$(46) \quad \tau_{1/2}(k_{\text{max}}) = \frac{\ln 2}{D_{\text{eff}} k_{\text{max}}^2} = \frac{\ln 2 \cdot h_{\text{elem}}^2}{\pi^2 D_{\text{eff}}} = \frac{\ln 2 \cdot h_{\text{elem}}^2}{\pi^2 C_{w0}/D} = \ln 2 \left( \frac{h_{\text{elem}}}{\pi} \right)^2 \frac{M_0 + \chi S_0/E_{ep}}{C_{w0}}.$$

540 We can ensure mesh-scale artifacts do not propagate through the discrete solution by enforcing that the  
 541 decay time is much shorter than the computational time step. The condition:

$$(47) \quad \tau_{1/2}(k_{\text{max}}) \ll \Delta t$$

542 guarantees that spurious high-frequency modes decay within a single time step. Herein, we propose a  
 543 quantification of this requirement; therefore, we demand that the mesh-scale mode amplitude decreases  
 544 to below 1/10,000 of its original size per time step (i.e., a reduction of at least 99.99%):

$$(48) \quad \boxed{e^{-D_{\text{eff}}(\pi/h_{\text{elem}})^2 \Delta t} = e^{[-(C_{w0}/(M_0 + \chi S_0/E_{ep}))(\pi/h_{\text{elem}})^2 \Delta t]} \lesssim 0.0001}$$

545 This criterion provides a direct relationship between material properties ( $D_{\text{eff}}$ ), spatial discretization  
 546 ( $h_{\text{elem}}$ ), and temporal discretization ( $\Delta t$ ) that ensures robust numerical performance.

547 **3.3. Load Rate Effects and Shear Bandwidth Control.** In quasi-static coupled analyses, the tem-  
 548 poral progression typically follows prescribed loading patterns rather than a physical time evolution.  
 549 The connection between load increments and time steps becomes:

$$(49) \quad \Delta t = \frac{\Delta \Sigma}{r},$$

550 where  $\Delta \Sigma$  represents the applied load increment and  $r$  denotes the loading rate. Substituting this  
 551 relation into the stability condition (48) and enforcing that  $\Delta t > \tau_{1/2}(k_{\text{max}})$ , allows us to solve for the

552 diffusion-induced characteristic length for the solution term with the longest wavelength:

$$(50) \quad \ell_c = \sqrt{\frac{\pi^2}{\ln 2} D_{\text{eff}} \frac{\Delta\Sigma}{r}} = \sqrt{\frac{\pi^2}{\ln 2} \frac{C_{w0}}{M_0 + \chi S_0/E_{ep}} \frac{\Delta\Sigma}{r}}$$

553 This scaling relation reveals how computational and physical parameters interact to determine localiza-  
554 tion characteristics. The equation establishes that the diffuse localization bandwidth depends on three  
555 key factors: the effective diffusion coefficient, the magnitude of the load increment, and the loading rate.

556 **Physical Interpretation of Parameter Dependencies.** The scaling relationship (50) provides prac-  
557 tical insight for modeling flow-liquefaction within the fully coupled calculation framework: larger load  
558 increments  $\Delta\Sigma$  lead to wider localization bands. We can physically interpret this finding since the sys-  
559 tem has more time to redistribute stresses and pressures before the next loading step. This temporal  
560 smoothing effect prevents the formation of extremely sharp gradients. Higher loading rates  $r$  produce  
561 narrower localization bands by reducing the time available for pressure redistribution between load incre-  
562 ments. Rapid loading approaches undrained conditions where pore pressures cannot equilibrate, leading  
563 to more localized failure patterns. The effective diffusion coefficient  $D_{\text{eff}}$  captures the material's intrinsic  
564 ability to redistribute pore pressure. Higher-permeability materials (larger  $D_{\text{eff}}$ ) exhibit broader local-  
565 ization bands because pressure gradients dissipate more readily. Conversely, low-permeability materials  
566 concentrate pore-pressure changes, thereby promoting sharper localization.

567 Although Eq. (50) is not intended as an empirical fit, the qualitative trends it predicts are consistent  
568 with experimental observations reported in the literature. Laboratory studies have examined the influ-  
569 ence of loading or strain rate on strain localization patterns in granular materials (Kodaka et al., 2005;  
570 Oka et al., 2006; Kodaka et al., 2007). Experimental investigations on sensitive clays (Gylland et al.,  
571 2013) further indicate that increasing loading rate promotes localized failure, whereas lower rates lead to  
572 barrel-shaped or more diffuse deformation patterns. While these observations are qualitatively consistent  
573 with the diffusion-controlled scaling proposed here, they should be interpreted with caution, as the avail-  
574 able experimental evidence remains limited and partly inconclusive, owing to the small number of tested  
575 specimens and the difficulty of independently varying permeability and loading rate while preserving  
576 identical material fabric, as well as isolating strain localization from boundary effects or buckling at high  
577 strain rates.

578 Similar regularization effects arising from hydromechanical coupling have been reported in dynamic  
579 settings where inertia and wave propagation play a central role (Schrefler et al., 1995; Zhang et al., 1999).  
580 In contrast, the present work addresses quasi-static flow-liquefaction problems. It derives a different scal-  
581 ing relationship, formulated in terms of similar physical parameters but governed by diffusion-controlled  
582 pore-pressure redistribution rather than inertial effects.

583 **Implementation Strategy and Quality Assurance.** In practice, these guidelines imply several steps.  
584 Before running simulations, modelers should evaluate the attenuation condition (48) to ensure adequate  
585 suppression of mesh-scale modes. This evaluation requires estimating the effective diffusion coefficient  
586 based on material properties and current loading conditions. For problems involving pore-pressure driven  
587 strain softening in which  $D_{\text{eff}}$  may vary significantly during loading, the time-step criterion should be  
588 evaluated using the minimum expected diffusion coefficient to ensure conservative estimates. Similarly,  
589 adaptive time-stepping schemes should monitor the effective diffusion coefficient and adjust the time in-  
590 crements accordingly. The bandwidth scaling relation (50) serves both as a predictive tool for estimating  
591 diffuse localization characteristics and as a quality check for numerical results. Computed localization  
592 widths should be consistent with the theoretical prediction, providing confidence in the accuracy of the  
593 solution.

594 **Extensions and Limitations.** These guidelines apply most directly to problems exhibiting diffusion-  
595 dominated behavior under hydrostatic conditions. When significant phase-drift effects or strong back-  
596 ground pressure gradients are present, the analysis becomes more complex, though the fundamental  
597 principles remain valid. For three-dimensional problems with anisotropic material properties, the ef-  
598 fective diffusion coefficient becomes direction-dependent, necessitating more sophisticated analysis to  
599 determine appropriate mesh and time-step sizes. However, the one-dimensional insights provide valuable  
600 guidance for establishing initial estimates and understanding the underlying physics. The regularization  
601 effect depends critically on maintaining adequate coupling between mechanical and hydraulic responses.  
602 *Numerical schemes that artificially decouple these fields or use inappropriate time integration methods*

603 *may not exhibit the expected mesh-independent behavior, highlighting the importance of consistent for-*  
 604 *mulation throughout the computational framework.*

605

## 4. FLOW-LIQUEFACTION UNDER A FULLY-COUPLED SCHEME

TABLE 1. HSsmall parameters for tailings.

Parameter	Unit	Value
Model	–	HSsmall
Unit weight, $\gamma$	kN/m <sup>3</sup>	21.0
Friction angle, $\phi'$	°	30
Cohesion, $c'$	kPa	0
Dilation angle, $\psi$	°	0
$G_0^{\text{ref}}$	MPa	40
$\gamma_{0.7}$	–	$10^{-4}$
$E_{ur}^{\text{ref}}$	MPa	75
$E_{50}^{\text{ref}}$	MPa	7
$E_{oed}^{\text{ref}}$	MPa	10
Stress dependency, $m$	–	0.5
Poisson's ratio, $\nu_{ur}$	–	0.25
OCR	–	1.00
$K_0^{nc}$	–	–
$R_{\text{inter}}$	–	0.95
Permeability, $k$	m/s	$1 \times 10^{-8}$

606 The numerical results presented below, spanning both laboratory-scale triaxial simulations and dam-  
 607 scale TSF analyses, demonstrate the influence of hydro-mechanical coupling on flow-liquefaction mod-  
 608 eling. Conventional uncoupled or purely mechanical approaches, long adopted in practice, are plagued  
 609 by mesh sensitivity and an inability to capture the reciprocal feedback between pore pressure and de-  
 610 formation. By contrast, the fully coupled formulation introduces diffusion-driven stabilization, which  
 611 regularizes strain localization and yields physically interpretable results across scales.

TABLE 2. Mesh-scale mode attenuation factors for varying time step sizes in coupled hydromechanical analysis (attenuation factors) computed using the stability criterion from (48) for representative material parameters: element size  $h_{\text{elem}} = 0.2$  mm and effective diffusion coefficient  $D_{\text{eff}} = 1.02 \times 10^{-9} \text{ m}^2\text{s}^{-1}$ ). The exponential argument  $-D_{\text{eff}}(\pi/h_{\text{elem}})^2 \Delta t$  quantifies the decay rate of the highest frequency mode resolvable by the mesh, while the attenuation factor represents the fraction of initial amplitude remaining after one time step. Time steps of 35 s or larger achieve attenuation below 0.01%, indicating effective suppression of spurious mesh-scale oscillations and ensuring mesh-independent diffuse localization patterns. Smaller time steps propagate high-frequency artifacts (up to 28% for  $\Delta t = 5$  s), leading to mesh-aligned failure bands that contaminate the physical solution.

$\Delta t$	$-D_{\text{eff}}(\pi/h_{\text{elem}})^2 \Delta t$	Spurious oscillations
40	–10.04	$4.3 \times 10^{-5}$ (0.004%)
35	–8.79	$1.5 \times 10^{-4}$ (0.01%)
30	–7.53	$5.3 \times 10^{-4}$ (0.05%)
25	–6.27	$1.8 \times 10^{-3}$ (0.1%)
20	–5.02	$6.5 \times 10^{-3}$ (0.6%)
15	–3.76	$2.4 \times 10^{-2}$ (2.3%)
10	–2.51	$8.1 \times 10^{-2}$ (8.1%)
5	–1.25	$2.8 \times 10^{-1}$ (28.4%)

## 612 4.1. Constitutive Model, Material Coupling, and Mesh Regularization.

613 **Constitutive Model and Material Description.** All simulations employ the Hardening Soil model  
 614 with small-strain stiffness (HSsmall), a widely adopted framework in geotechnical analysis that captures  
 615 the nonlinear stress–strain behavior of granular and tailings materials. While critical-state models, such  
 616 as NorSand, would be expected to provide a more detailed description of post-peak and post-trigger  
 617 shear band development, these models are not readily available or robustly implemented within fully  
 618 coupled flow–deformation formulations that incorporate unsaturated flow, as required for the type of  
 619 analyses addressed in this paper. The present study adopts HSsmall as a pragmatic and widely used  
 620 choice to investigate the regularization effects arising from fully coupled flow–deformation formulations,  
 621 which are not expected to be qualitatively altered by the specific constitutive model employed, provided  
 622 that a consistent constitutive tangent operator exists for the linearization of the governing equations.

623 The parameter set (Table 1) corresponds to a contractive tailings material prone to pore-pressure  
 624 driven softening during rapid loading, calibrated to reproduce the responses of loose, saturated tailings  
 625 susceptible to flow liquefaction.

626 The HSsmall formulation incorporates a small-strain shear stiffness  $G_0^{\text{ref}}$ , which controls the onset of  
 627 stiffness weakening, and reference moduli  $E_{50}^{\text{ref}}$ ,  $E_{\text{oed}}^{\text{ref}}$ , and  $E_{\text{ur}}^{\text{ref}}$  governing deviatoric stiffness, oedometric  
 628 compression, and unloading–reloading, respectively. The stiffness exponent  $m$  describes stress depen-  
 629 dency, while the strain threshold  $\gamma_{0.7}$  governs small-strain decay. Yield and plastic potential surfaces  
 630 are also controlled by  $\phi'$ ,  $\psi$ , and the interface reduction factor  $R_{\text{inter}}$ . Finally, permeability  $k$  governs  
 631 pore-pressure diffusion, making it central to the stabilizing mechanism inherent in coupled analyses.

TABLE 3. Van Genuchten parameters for tailings.

Parameter	Unit	Value
Model	–	Van Genuchten
$S_{res}$	–	6.83%
$S_{sat}$	–	100%
$g_n$	–	3.00
$g_a$	1/m	4.30
$g_l$	–	1.25

632 Unsaturated conditions are accounted for within the fully coupled flow–deformation and effective stress  
 633 formulation, whereby matric suction is linked to the degree of saturation and, consequently, the storage  
 634 and diffusion terms in Eqs. (4) and (5). This affects pore-pressure evolution within localized deformation  
 635 zones without introducing additional mechanical dissipation. The parameter set (Table 3) was selected  
 636 to limit the influence of suction (F. Lopez Rivarola, 2023) and to improve numerical convergence of the  
 637 flow problem. A detailed calibration of suction-dependent hydraulic parameters is beyond the scope of  
 638 the present study.

#### 639 4.2. Triaxial Test.

640 **Simulation setup.** The triaxial test provides a controlled environment for examining the mesh-  
 641 regularization effect predicted in Section 3.2. We simulate an isotropically consolidated undrained (CIU)  
 642 specimen using a two-dimensional axisymmetric finite element model. The cylindrical sample has a  
 643 radius of 5 mm, a height of 10 mm, and is discretized with uniform elements of size  $h_{\text{elem}} = 0.2$  mm.  
 644 Rough ends prevent radial displacement, while a prescribed vertical displacement imposes a constant  
 645 axial strain rate of  $\frac{1}{180}$  %/s in all cases. The loading sequence comprises three stages: (i) isotropic con-  
 646 solidation to  $p' = 600$  kPa under drained conditions; (ii) switch to undrained mode with displacement  
 647 reset; and (iii) axial straining up to  $\varepsilon_y = 20\%$  under fully coupled conditions at the same load rate with  
 648 impermeable boundaries. Eight fully coupled analyses were performed using time-step increments,

$$\Delta t \in \{40, 35, 30, 25, 20, 15, 10, 5\} \text{ s,}$$

649 and compared them with a reference *undrained plastic* calculation—i.e., a purely mechanical analysis  
 650 where the mass balance equations are not solved, and excess pore pressures are generated directly from  
 651 the constitutive undrained response rather than from transient fluid flow. Here, parameters presented  
 652 in Table 1 were used to compute the effective diffusion coefficient, and a fully saturated material with a  
 653 permeability of  $1 \times 10^{-12}$  m/s, obtaining a final value of  $D_{\text{eff}} = 1.02 \times 10^{-9} \text{ m}^2\text{s}^{-1}$ . Table 2 reports the  
 654 predicted attenuation factors, computed using (48). Since the finite element mesh imposes a maximum  
 655 resolvable wavenumber  $k_{\text{max}} = \pi/h_{\text{elem}}$ , any wavenumber above this value is non-physical and can  
 656 corrupt the solution. These mesh-scale perturbations decay exponentially with a characteristic time

657  $\tau_{1/2}(k_{\max}) \propto h_{\text{elem}}^2/D_{\text{eff}}$ , governed by the effective diffusion coefficient. Thus, we suppress these spurious  
 658 oscillations by limiting the time step  $\Delta t$  to be  $e^{-D_{\text{eff}}(\pi/h_{\text{elem}})^2\Delta t} \lesssim 0.0001$ , ensuring that nonphysical  
 659 modes decay by at least 99.99% within one step.

660 Figures 1-3 summarize the numerical results of the triaxial tests. Stress-strain curves collapse onto  
 661 a single envelope for a fully coupled scheme, following a similar pattern shown by a single point simulation  
 662 (soil test), whereas uncoupled (plastic) calculation leads to an early pore-pressure driven softening  
 663 response and the emergence of element-scale shear bands on top of larger wave-length solutions which  
 664 drives the typical barrel-shaped failure in loose tailings (see Figure 2 (a) and (b)). Yet, even when lower-  
 665 wavelength shear bands are propagated, the global stress-strain behavior remains within engineering  
 666 tolerance, albeit with evident mesh sensitivity due to the dominance of the larger-wavelength solutions.

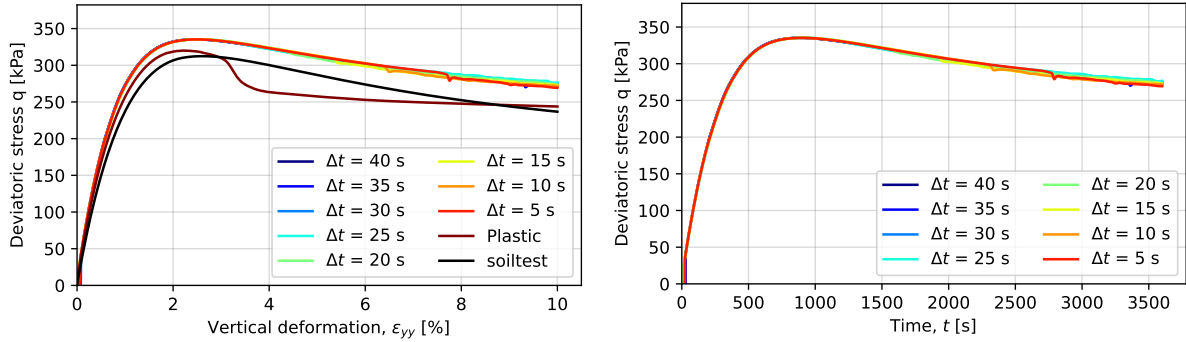
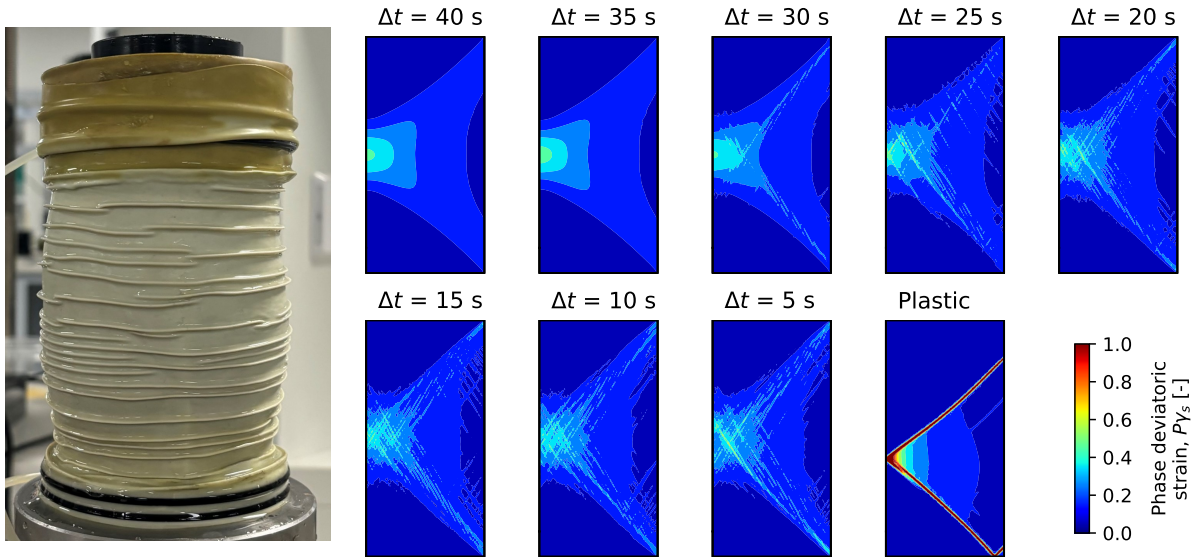


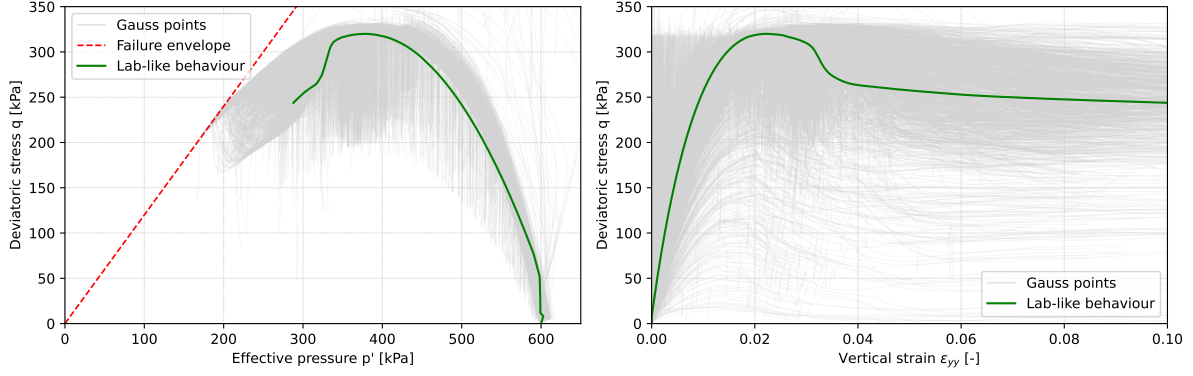
FIGURE 1. Stress-strain response from fully coupled triaxial tests. Deviatoric stress versus axial strain (left) & time (right). All curves converge to a common envelope, confirming mesh-independence and reproducing a shape similar to that obtained from a single-point calculation (soil test). Plastic calculations lead to mesh dependency.



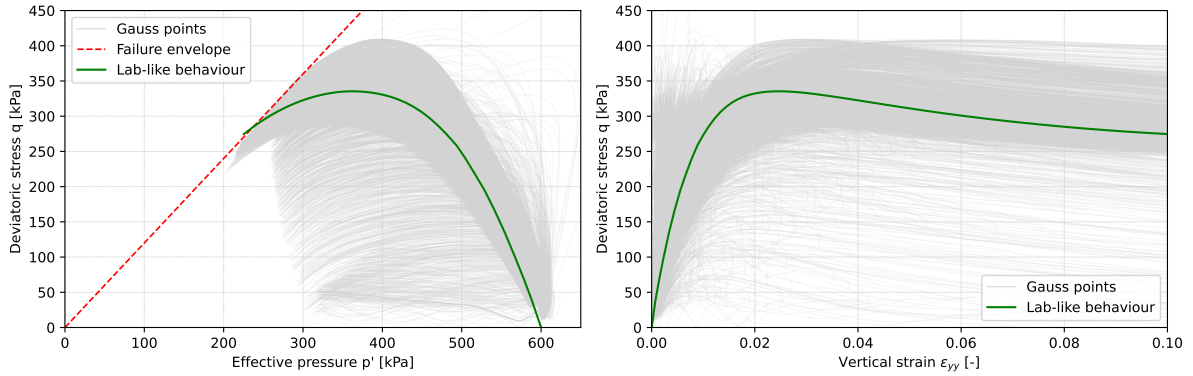
(A) Diffuse barrel-shaped failure of loose tailings.

(B) Shear strain contours for an undrained triaxial test.

FIGURE 2. Shear-band formation in fully coupled triaxial tests compared with a sampled test at the laboratory: critical role of time step filtering in localization patterns. Deformation fields at  $\varepsilon_{yy} = 20\%$  reveal distinct morphological transitions controlled by the temporal discretization parameter  $\Delta t$ . For time steps exceeding 35 s, the system yields larger-wavelength solutions, whereas smaller time increments ( $\Delta t < 35$  s) produce spurious multiple bands aligned with the finite element mesh, representing unresolved short-wavelength perturbations that contaminate the physical solution.



(A) Uncoupled plastic calculation. Gauss-point trajectories scatter broadly around the bulk response, with many overshooting the failure envelope before pore-pressure driven softening. Unloading paths are frequent, signaling bifurcation and severe localization. Local peak deviatoric stresses approach  $\approx 330$  kPa, exceeding the averaged maximum of  $\approx 310$  kPa. The  $q-\varepsilon_y$  curve shows similar divergence: while the averaged response peaks at  $\varepsilon_y \approx 0.02$ , individual points follow disparate paths, some pore-pressure driven softening rapidly while others continue straining almost elastically.



(B) Fully coupled calculation with  $\Delta t = 40$  s. The  $q-p$  scatter contracts around the bulk curve, and unloading trajectories nearly vanish. Diffusion redistributes stresses, suppresses local overstressing, and promotes uniform energy dissipation across the specimen. In  $q-\varepsilon_y$  space, the scatter narrows, with the averaged curve bounding nearly all Gauss-point responses. The outcome is a smoother, mesh-independent, and rate-insensitive pore-pressure driven softening branch. Time-step size enforcement suppresses local overstressing and avoids unphysical responses.

FIGURE 3. Stress-strain paths at Gauss points vs averaged specimen response

667 **Local versus global behavior.** Figure 3 contrasts the global specimen response and Gauss-point stress  
 668 paths. In the uncoupled plasticity calculation, integration points are distributed widely, with many  
 669 overshooting the failure envelope before pore-pressure driven softening, thereby producing unloading  
 670 paths and bifurcation signatures. During the pore-pressure driven softening, points outside the shear  
 671 band begin to unload elastically. Because of the imposed undrained condition ( $\varepsilon_v = 0$ ) the mean effective  
 672 pressure remains constant during unloading, and the stress path drops vertically in the  $q-p$  plane as shear  
 673 stress decreases. Local peak deviatoric stresses approach  $\approx 330$  kPa, even as the averaged curve peaks  
 674 nearer  $\approx 310$  kPa. Similarly, while the global  $q-\varepsilon_y$  curve peaks around  $\varepsilon_y \approx 0.02$ , individual Gauss  
 675 points follow divergent paths, with some rapidly dropping deviatoric stress and others straining almost  
 676 elastically. Severe localization is thus hidden beneath the smooth green envelope. With full coupling and  
 677  $\Delta t = 40$  s, the picture changes. The  $q-p$  scatter contracts around the bulk curve, unloading trajectories  
 678 nearly vanish, and energy dissipation is distributed more uniformly. The  $q-\varepsilon_y$  scatter also narrows,  
 679 with the averaged curve bounding nearly all point responses. Diffusion suppresses local overstressing,  
 680 aligning microscopic and macroscopic behavior. The outcome is a smoother, mesh-independent, rate-insensitive  
 681 pore-pressure driven softening branch.

682 **Interpretation & broader perspective.** Together, these results show that coupling momentum and  
 683 mass balance equations regularizes the pore-pressure driven softening response. Pore-pressure diffusion

684 acts as an implicit viscous-like mechanism, resisting abrupt volumetric changes, damping high-frequency  
 685 perturbations, and imposing a diffuse finite localization width. When the time step is sufficiently large,  
 686 this filtering dominates, thereby avoiding mesh-dependent solutions. For very small time-step increments,  
 687 unresolved modes survive, shear bands fragment, and mesh dependence dominates the shear contours.

688 **Remark 4. Shear-band morphology.** Localization patterns at  $\varepsilon_{yy} = 20\%$  (Figure 2) reveal the spatial  
 689 expression of this filtering. For  $\Delta t > 35$  s, deformation organizes into a single barrel-shaped shear band,  
 690 in agreement with experimental triaxial tests for loose tailings samples. For smaller increments, mul-  
 691 tiple element-aligned bands appear, a direct manifestation of unresolved short-wavelength perturbations.  
 692 Interpreted through the morphing-pattern framework (Regenauer-Lieb et al., 2025a,b), the distinction  
 693 reflects whether the system locks onto a dominant wavelength or permits the coexistence of competing  
 694 instabilities. In the limit case of an uncoupled plastic calculation, a unique shear band propagates, which  
 695 does not correspond to the experimental evidence for loose tailings undergoing flow-liquefaction.

696 Seen through the lens of morphing patterns, the triaxial results embody a universal instability mech-  
 697 anism. Strong attenuation favors the selection of a single coherent shear band—a stable morphology.  
 698 Weak attenuation allows multiple short bands, reflecting the competition of unstable modes. This mirrors  
 699 Turing-type instabilities, in which the emergent wavelength depends on the balance between local ampli-  
 700 fication and diffusion. The triaxial test thus goes beyond validating a numerical criterion: it illustrates  
 701 how hydro-mechanical coupling shapes the geometry of failure, linking internal diffusion with external  
 702 loading to produce physically consistent diffuse localization patterns in geomaterials.

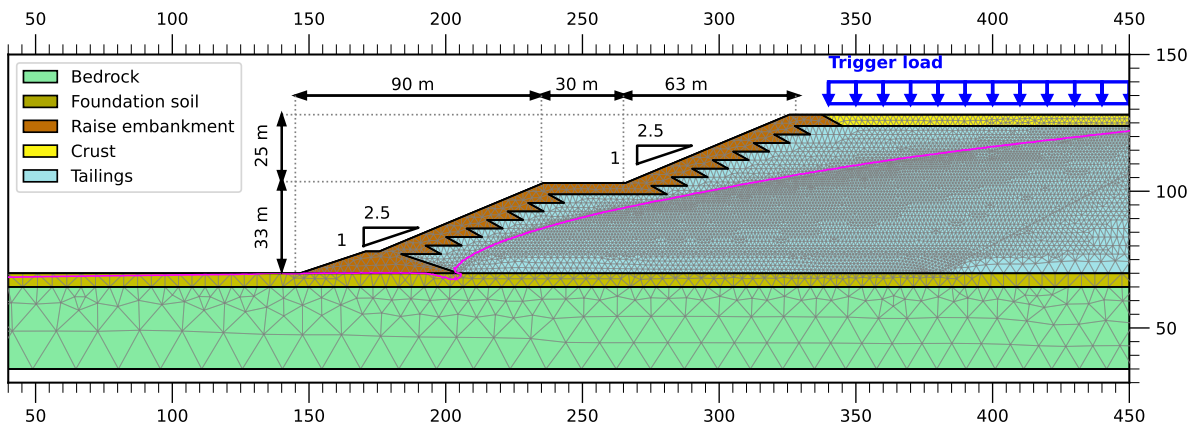


FIGURE 4. Geometry of the upstream-raised TSF model and trigger load.

703 **4.3. TSF Flow-liquefaction Analysis.** The second set of analyses extends the study from the element  
 704 scale to the field scale, focusing on the vulnerability of a Tailings Storage Facility (TSF) to flow lique-  
 705 faction. The framework follows the methodology (Ledesma et al., 2022) and adopts the representative  
 706 configuration proposed by (Tasso et al., 2024). Figure 4 shows the model geometry, principal geotechnical  
 707 units, and trigger load considered for the assessment. The geometry corresponds to a hypothetical  
 708 upstream-raised TSF with a total height of 58 m, a mid-height berm, and overall slope gradients of  
 709 1V : 2.5H. The stratigraphy includes foundation soils, embankment material, and contractive tailings,  
 710 underlain by bedrock. Average mesh size on materials prone to fail, i.e., tailings and embankments, is  
 711  $h_{\text{elem}} \approx 0.75$  m.

712 We simulate the construction in staged raises of 3.0 m at a rise rate of 2.0 m/year. This staged  
 713 procedure is crucial for reproducing the stress redistribution and pore-pressure evolution that govern  
 714 the in situ state prior to triggering. Unlike simplified monotonic loading schemes, staged construction  
 715 generates a non-uniform stress field and establishes a realistic phreatic surface position, both of which  
 716 strongly influence liquefaction susceptibility. The fully coupled hydro-mechanical formulation proves  
 717 essential in this context. By solving simultaneously for displacements and pore pressure, the scheme  
 718 captures the competition among deformation, staged-construction effects, and pore-pressure diffusion.  
 719 In particular, it enables assessment of partially drained triggers, in which the hydraulic conductivity  
 720 of the tailings determines whether loading conditions result in drained, partially drained, or undrained  
 721 behavior.

TABLE 4. Parametric sweep on external load rate  $r$  influence on liquefaction triggering. Columns report: applied load rate, failure time  $t_f$ , numerical time-step size  $\Delta t$ , imposed load increment  $\Delta\Sigma$ , predicted trigger load, and dimensionless velocity. For extremely slow rates ( $r \leq 2 \times 10^{-7}$  kPa/s), diffusion keeps pace with loading, leading to near-drained behavior. Failure times extend to several years ( $t_f \sim 10^{10}$  s), and the system resists liquefaction until very high stresses ( $\gtrsim 1100$  kPa). As  $r$  increases, pore-pressure diffusion lags progressively behind loading, shortening  $t_f$  and reducing the trigger load. This trend continues until a plateau emerges for  $r \geq 0.2$  kPa/s, where further rate increases no longer affect the response. Thus, the system converges to the undrained limit, with triggering loads stabilizing at approximately 150 kPa. The intermediate line in the table represents a transition point at which the failure becomes drained-like-dominated. Dimensionless velocity also converges into a fixed value on the limits, being  $\sim 0.024$  for drained and  $\sim 0.165$  for undrained.

Load rate $r$ [kPa/s]	Failure time $t_f$ [s]	Step size $\Delta t$ [s]	Load increment $\Delta\Sigma$ [kPa]	Trigger load [kPa]	Dimensionless velocity $\ell_c^2/(t_f D_{\text{eff}})$ [-]
0.000 000 002	589 800 000 000.0	100 000 000	2	1179.6	0.024
0.000 000 02	58 979 200 000.0	10 000 000	2	1179.6	0.024
0.000 000 2	5 700 000 000.0	10 000 000	2	1140.0	0.024
0.000 002	529 688 000.0	1 000 000	2	1059.3	0.026
0.000 004	244 785 000.0	500 000	2	979.1	0.029
0.000 01	91 770 000.0	200 000	2	917.7	0.031
0.000 02	32 895 500.0	100 000	2	677.9	0.043
0.000 04	12 484 050.0	50 000	2	499.3	0.057
0.0001	3 197 380.0	20 000	2	319.7	0.089
0.0002	1 290 790.0	10 000	2	258.1	0.110
0.002	97 727.0	1000	2	195.4	0.145
0.02	8845.9	100	2	176.9	0.160
0.2	868.6	10	2	153.7	0.163
2.0	85.82	1	2	151.6	0.165
20.0	8.61	0.1	2	152.3	0.165
200.0	0.86	0.01	2	152.4	0.165

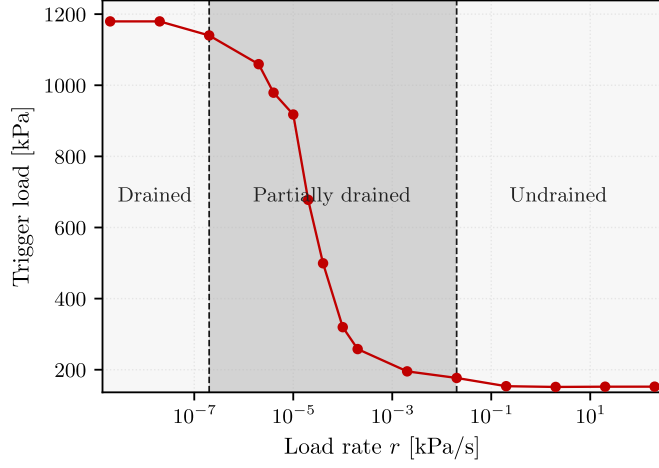
722 **4.4. Influence of Load Rate  $r$  on Diffuse Localization Bandwidth.** The external load rate  $r$  plays  
723 a decisive role in governing the competition between hydraulic diffusion and mechanical pore-pressure  
724 driven softening. In fully coupled analyses, pseudo-time is defined by the applied load history, such that  
725 the increment length is

$$\Delta t = \frac{\Delta\Sigma}{r},$$

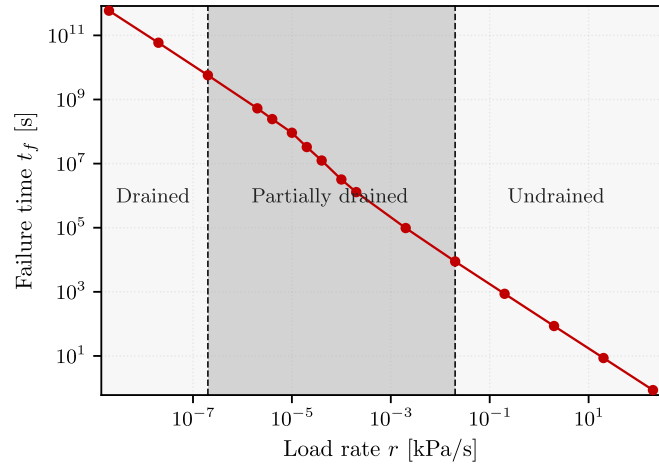
726 where  $\Delta\Sigma$  is the prescribed load increment per step. Consequently, both  $\Delta\Sigma$  and  $r$  control the effective  
727 diffusion length  $\ell_c \sim \sqrt{D_{\text{eff}} \Delta t}$  and, by extension, the width of the shear localization zone.

728 Table 4 summarizes the parametric sweep. For extremely slow rates ( $r \leq 2 \times 10^{-7}$  kPa/s), the system  
729 experiences near-drained conditions: diffusion keeps pace with loading, failure times exceed several years  
730 ( $t_f \sim 10^{10}$  s), and triggering occurs at high stresses exceeding 1100 kPa. As the rate increases, drainage  
731 lags progressively behind, leading to a steady reduction in the triggering load. This trend continues until  
732 a plateau is reached near  $r \geq 0.2$  kPa/s, where further rate increases no longer alter the failure load. At  
733 this point, the response converges to the undrained limit, with triggering loads around 150 kPa.

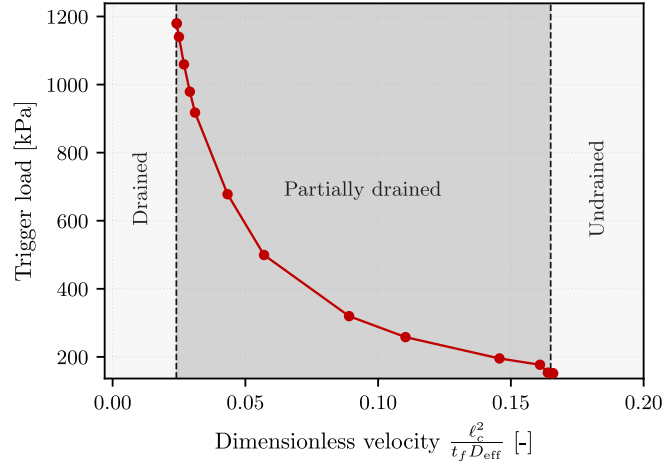
734 On the other hand, the dimensionless parameter  $\ell_c^2/(t_f D_{\text{eff}})$  is also introduced, describing the type of  
735 tailing drainage during failure. The dimensionless velocity shows a value of  $\sim 0.024$  for drained triggers,  
736 while it is increased to  $\sim 0.165$  when reaching undrained behavior, with a transitioning zone in between  
737 for partially drained triggers.



(A) Load rate versus trigger load.



(B) Load rate versus time at failure.



(C) Trigger load versus dimensionless velocity.

FIGURE 5. Drained-to-undrained transition as a function of the external load rate  $r$ . (a) Trigger load decreases sharply with increasing  $r$ , approaching a drained asymptote at slow rates and an undrained asymptote at fast rates. (b) Failure time follows an inverse power-law scaling, with slopes consistent with our spectral forecast of the diffusion length  $\ell_c$ . (c) Dimensionless velocity shows a wide span for partially drained triggers, whereas it converges to fixed values on the drained and undrained limits. Together, the curves demonstrate the natural-rate dependence of hydro-mechanical coupling: rapid loading suppresses diffusion and promotes sharp, narrow shear bands, whereas slow loading allows dissipation and broadens the localization zone.

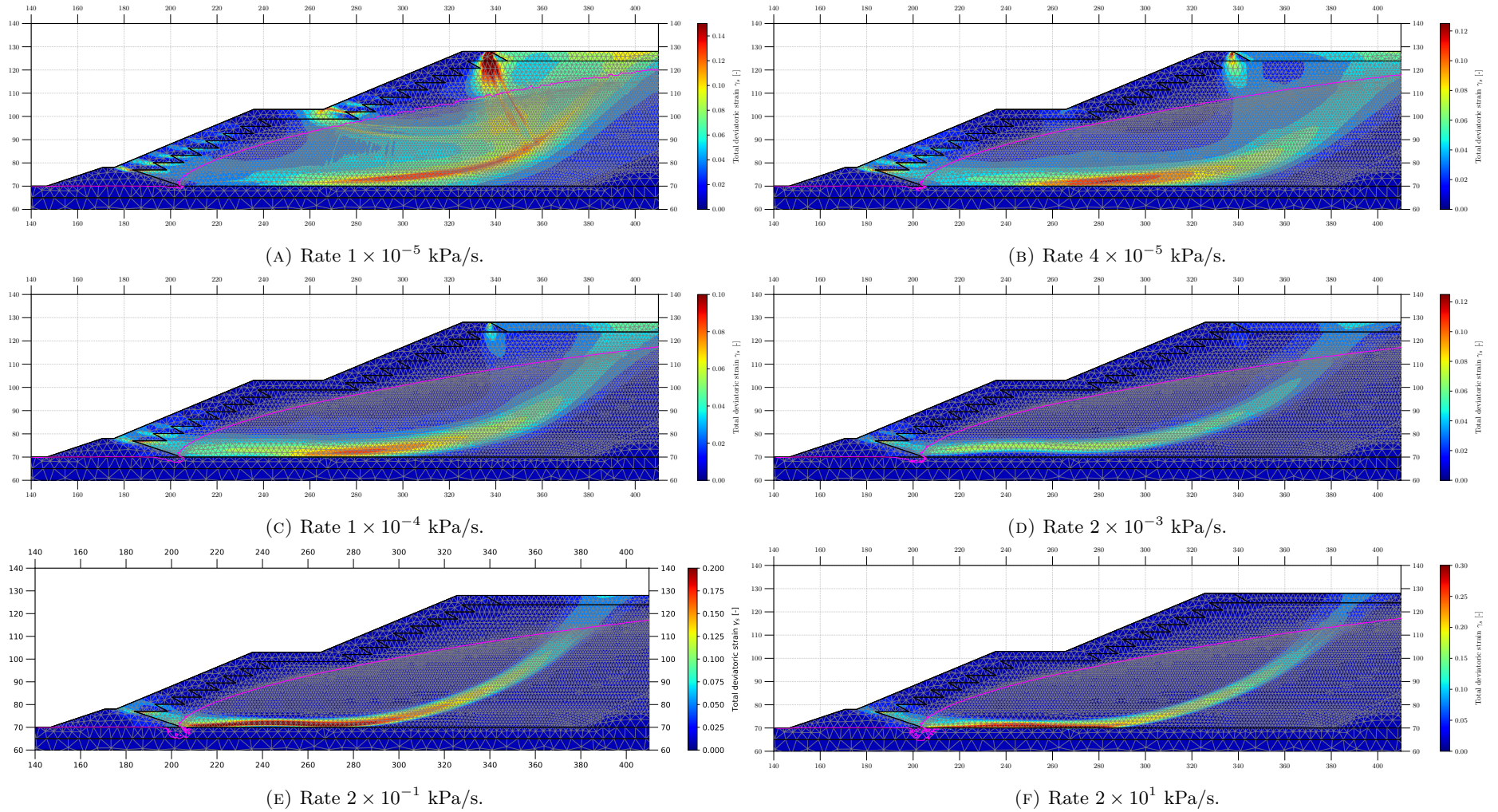


FIGURE 6. Shear-band morphology as a function of external load rate  $r$ . At slow rates ( $r \sim 10^{-5}$  kPa/s), deformation is broad and diffuse, reflecting the limit of drained-like behavior with close to continuous pore-pressure equilibration. Intermediate rates ( $r \sim 10^{-5}$ – $10^{-3}$  kPa/s) yield transitional patterns: shear bands narrow, pore pressures partially accumulate, and the trigger load decreases sharply. At high rates ( $r \geq 0.002$  kPa/s), localization collapses into thin, well-defined bands with concentrated pore-pressure excess, similar to fully undrained responses.

738 Figure 5 illustrates this transition in terms of trigger load versus load rate, time at failure versus load  
 739 rate, and trigger load versus dimensionless velocity. The curve of trigger load versus rate shows a sharp  
 740 decline over several orders of magnitude in timescale, bounded by a drained asymptote at slow rates and  
 741 an undrained asymptote at fast rates. The failure time, plotted against  $r$ , follows an inverse scaling,  
 742 with log–log slopes that match the spectral predictions of  $\ell_c$ . The dimensionless velocity varies widely  
 743 for partially drained triggers, whereas at the limits it remains constant. These results demonstrate that  
 744 hydro-mechanical coupling introduces a natural rate dependence: the faster the external load is applied,  
 745 the narrower the diffusion bandwidth and the sharper the strain localization.

746 The deformation patterns shown in Figure 6 reinforce this interpretation. At slow rates ( $r \sim$   
 747  $10^{-5}$  kPa/s), deformation is broad and diffuse, reflecting the limit of drained-like behavior with close  
 748 to continuous pore-pressure equilibration. Intermediate rates ( $r \sim 10^{-5}$ – $10^{-3}$  kPa/s) produce transi-  
 749 tional behavior: shear zones narrow down, pore pressures partially accumulate, and the trigger load  
 750 drops rapidly. At high rates ( $r \geq 0.2$  kPa/s), deformation collapses into thin, well-defined bands, and  
 751 excess pore pressures concentrate sharply, mimicking a fully undrained response.

752 Taken together, these findings highlight the sensitivity of liquefaction analyses to the choice of ex-  
 753 ternal loading rate. In practice, this underscores the importance of relating numerical rate parameters  
 754 to plausible field scenarios. Overly slow numerical rates may exaggerate stability margins by implicitly  
 755 permitting drainage, while excessively fast rates may underestimate them by enforcing undrained con-  
 756 ditions. Reliable assessments, therefore, require loading rates consistent with the expected timescales of  
 757 seismic shaking, operational loading, or other relevant triggers.

TABLE 5. Influence of hydraulic permeability on instability trigger loads in coupled triaxial compression tests. A clear transition from partially drained to fully undrained mechanical response occurs as the permeability decreases. At  $k = 10^{-8}$  m/s, the trigger load reaches 177 kPa, indicating partially drained conditions, as pore-pressure dissipation delays failure onset and requires higher applied stresses. As permeability decreases to  $10^{-10}$  m/s and below, trigger loads converge to approximately 158 kPa, indicating the transition to fully undrained behavior. The asymptotic plateau for permeabilities below  $10^{-10}$  m/s confirms that diffusive time scales are longer than loading time scales, effectively decoupling hydraulic and mechanical responses.

Permeability [m/s]	Trigger load [kPa]
$1 \times 10^{-4}$	1078.78
$1 \times 10^{-6}$	255.45
$1 \times 10^{-8}$	176.92
$1 \times 10^{-10}$	159.10
$1 \times 10^{-11}$	158.21
$1 \times 10^{-12}$	158.16
$1 \times 10^{-14}$	158.51
$1 \times 10^{-20}$	158.35

758 **4.5. Influence of Permeability on Diffuse Localization Bandwidth.** Permeability governs the  
 759 ability of pore water to dissipate pressure during loading and, in fully coupled analyses, directly controls  
 760 the internal diffusion length scale that regularizes strain localization. According to the scaling relation  
 761 for  $\ell_c$  of (50), where  $D_{\text{eff}} = \frac{C_{w0}}{M_0 + \chi S_0/E_{ep}}$  is proportional to  $k/\mu$ , higher permeabilities enlarge the  
 762 diffusion length, broaden shear bands, and delay the onset of instability. Conversely, low permeabilities  
 763 suppress diffusion, forcing the system towards an undrained response characterized by narrow, sharply  
 764 localized deformation and rapid pore-pressure build-up.

765 Table 5 summarizes the trigger loads obtained for different permeabilities. The trend is clear: when  
 766 permeabilities are higher than  $k = 10^{-8}$  m/s, the triggering load grows to values greater than in the  
 767 nearly undrained cases ( $\approx 158$  kPa). However, once permeability decreases below  $10^{-10}$  m/s, the response  
 768 plateaus, with only minor variations in the triggering load. This asymptotic behavior confirms that below  
 769 a critical permeability threshold, diffusion is too slow to affect the macroscopic response. The system  
 770 behaves as fully undrained (i.e., a critical permeability threshold exists below which the system exhibits  
 771 a purely undrained mechanical response, regardless of further permeability reduction, with variations of  
 772 less than 1 kPa (0.6%) across a four-order-of-magnitude permeability reduction).

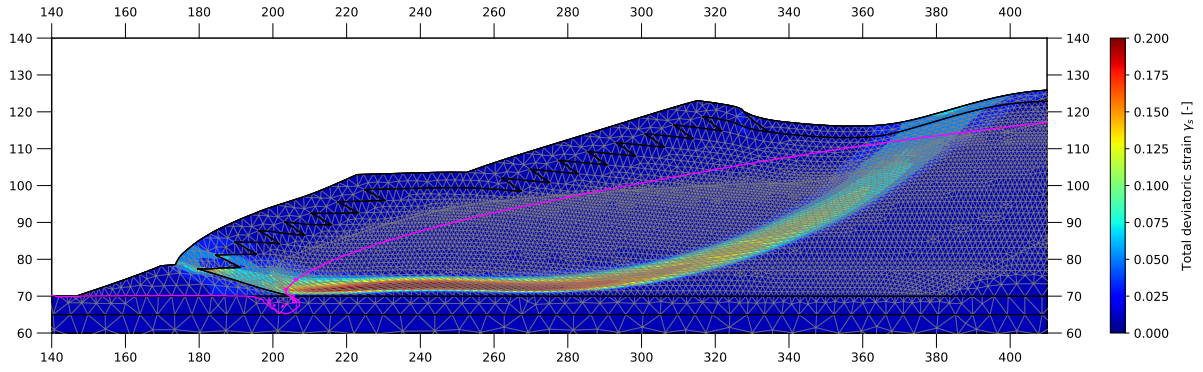
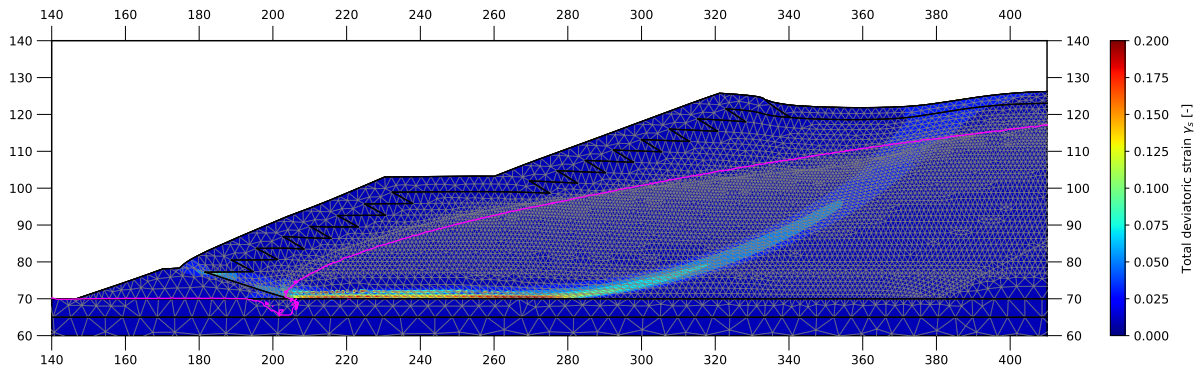
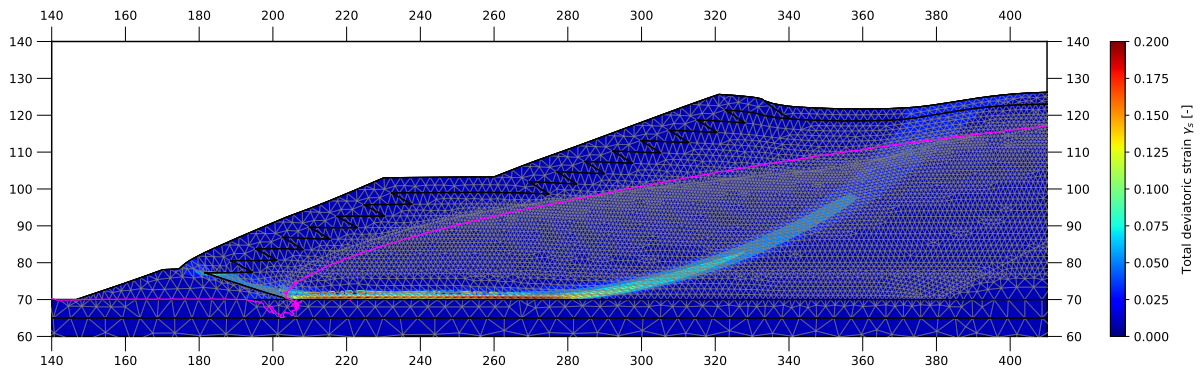
(A) Permeability  $k = 1 \times 10^{-8}$  m/s.(B) Permeability  $k = 1 \times 10^{-10}$  m/s.(C) Permeability  $k = 1 \times 10^{-20}$  m/s.

FIGURE 7. Influence of permeability on shear-band morphology in liquefaction. At  $k = 10^{-8}$  m/s, shear localization is broad and diffuse, reflecting efficient stress redistribution through fluid flow. As permeability decreases to  $k = 10^{-10}$  m/s and below, shear bands progressively sharpen and concentrate along critical stress trajectories, reflecting the material's reduced ability to dissipate pore-pressure gradients. In the very low-permeability regime, deformation collapses into narrow, sharply defined zones, consistent with an undrained limit. The results show a  $10\times$  deformation magnification.

773 Figures 7 and 8 illustrate the associated deformation and pore-pressure fields. In higher-permeability  
 774 cases, shear localization is diffuse, spanning broad regions with a gradual stress redistribution. As per-  
 775 meability decreases, bands sharpen and align along critical stress paths, with deformation concentrating  
 776 into thin shear zones. At the same time, excess pore pressures intensify and become less uniformly dis-  
 777 tributed, reflecting the system's reduced ability to dissipate hydraulic gradients. The low- $k$  simulations  
 778 highlight that the coupled formulation naturally recovers the undrained limit without requiring artificial  
 779 boundary conditions or uncoupled assumptions.

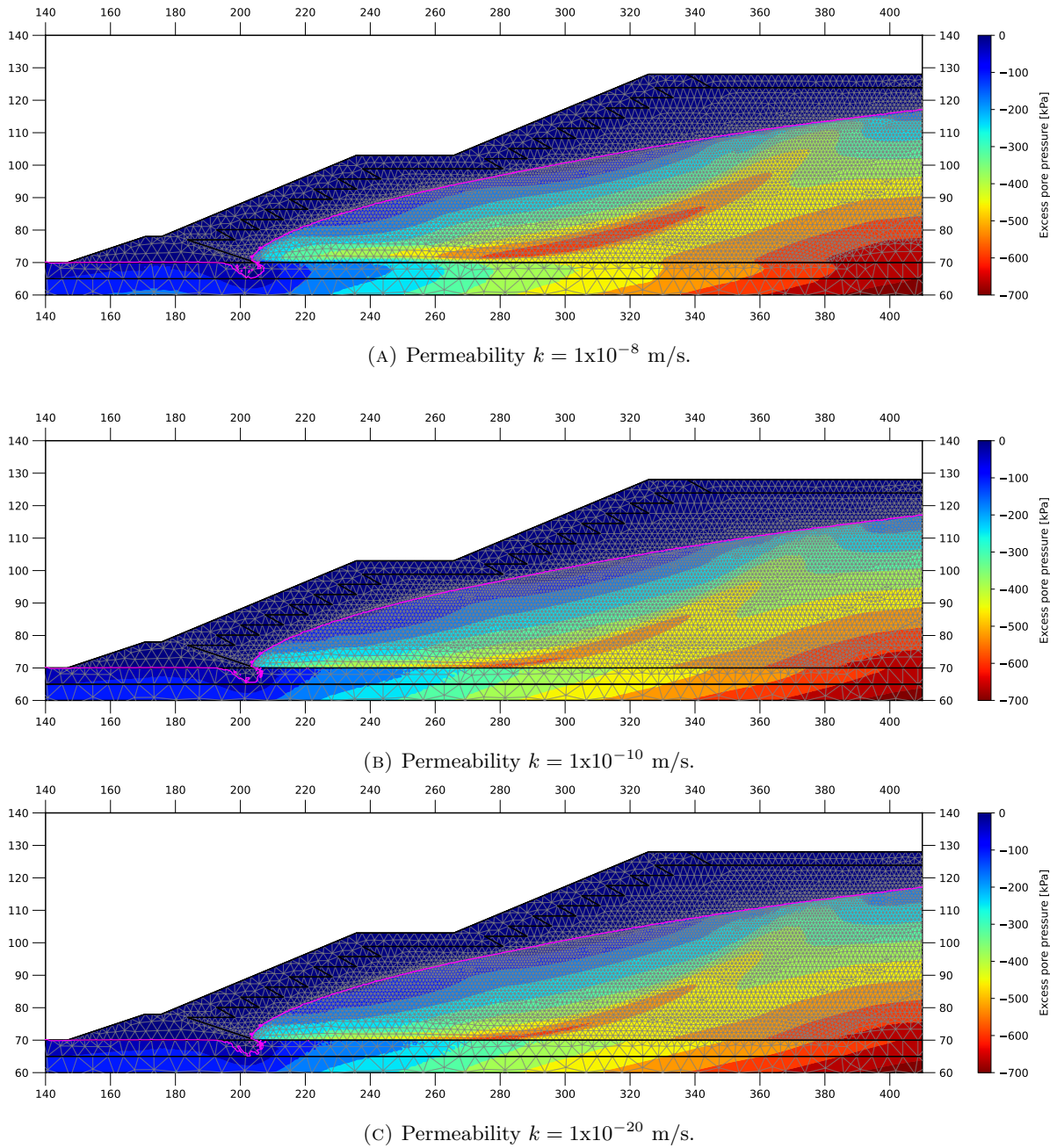
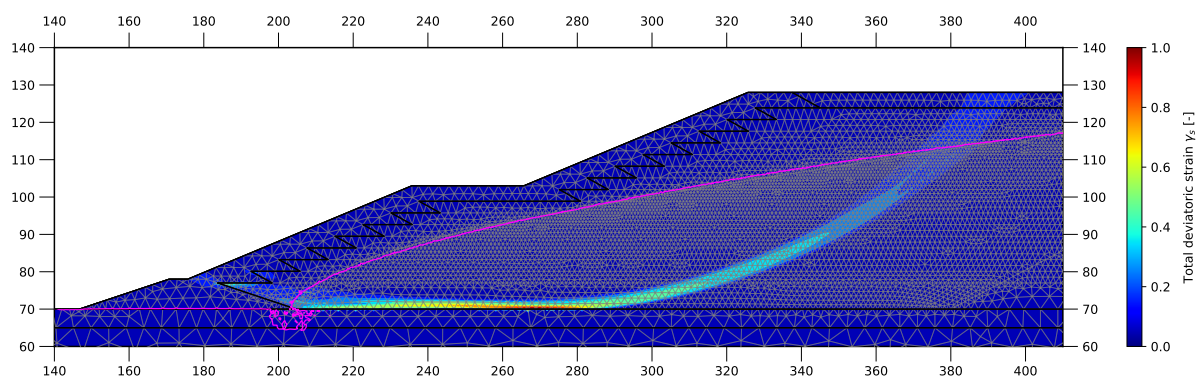
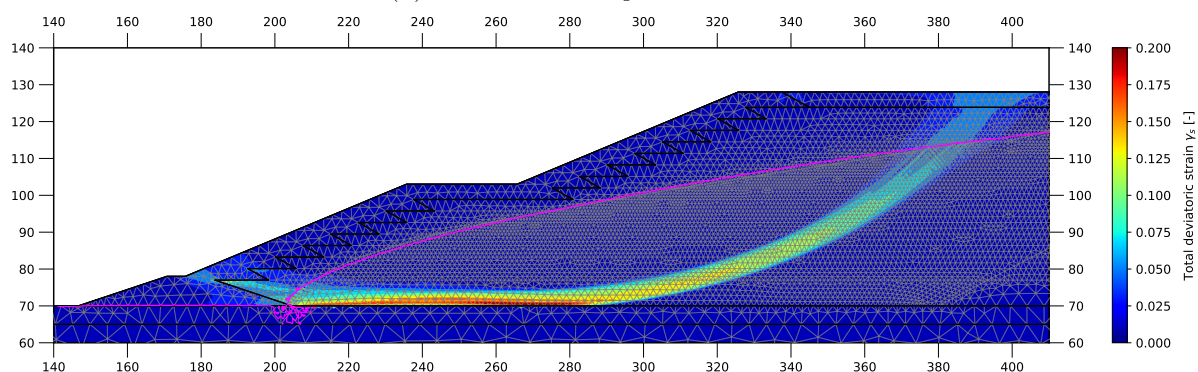


FIGURE 8. Influence of permeability on excess pore-water pressure at the liquefaction phase. For  $k = 10^{-8}$  m/s, pore-pressure excesses remain modest and spatially diffuse, consistent with efficient hydraulic dissipation. As permeability decreases, excess pore pressures grow and concentrate into smaller zones, amplifying contractive tendencies in the tailings. At very low permeabilities, dissipation is negligible, producing sharp gradients and large pressure build-ups characteristic of fully undrained conditions.

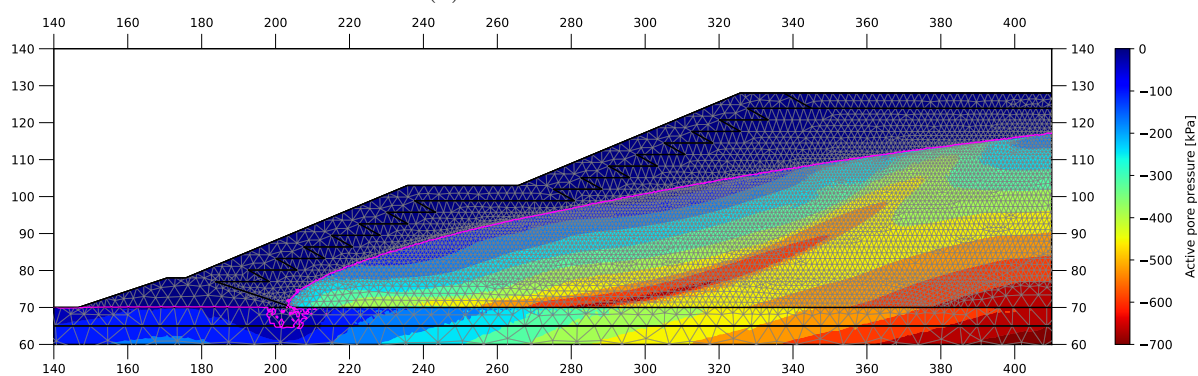
780 These results demonstrate that permeability not only dictates the overall stability margin, but also  
 781 the width of shear localization zones and the spatial pattern of pore-pressure excess. In practical terms,  
 782 this highlights the importance of carefully characterizing the permeability of tailings materials. Small  
 783 variations in  $k$  near the critical threshold can shift the response from drained to undrained, significantly  
 784 altering the apparent safety margin of a TSF. Beyond this threshold, however, further decreases in  $k$   
 785 have a negligible effect on global stability, suggesting that engineering assessments should focus on the  
 786 transitional range in which drainage conditions are neither fully active nor fully suppressed.



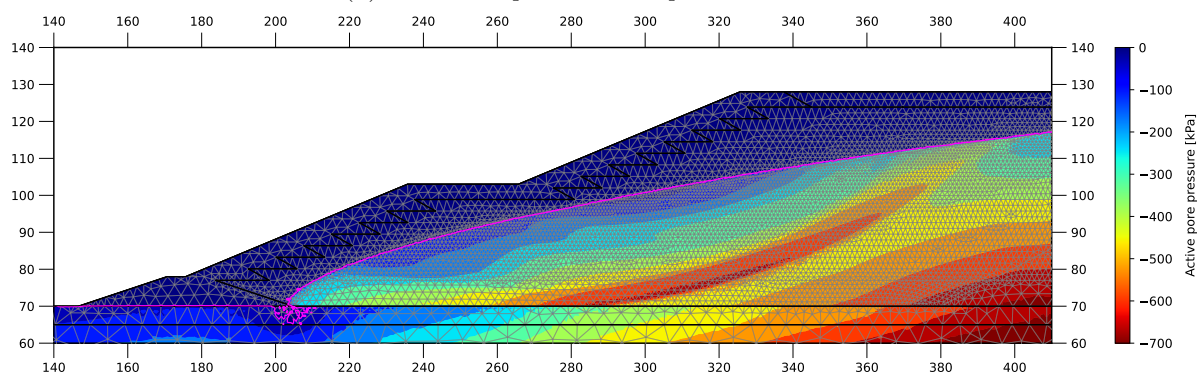
(A) Shear band - compressible material.



(B) Shear band - stiffer material.



(C) Pore water pressure - compressible material.



(D) Pore water pressure - stiffer material.

FIGURE 9. Material compressibility effect on the shear band morphology. Compressible materials generate pore water pressure, which dissipates more slowly than stiffer materials, generating a narrower high-pressure band and, consequently, a narrower shear band.

TABLE 6. Influence of compressibility on instability trigger loads in the analysed TSF section. Results show an increase in the flow-liquefaction trigger load as oedometric stiffness increases, due to a lag in pore water pressure generation.

$E_{oed}^{ref}$ [MPa]	Trigger load [kPa]
$E_{oed}^{ref} \times 0.5$	170.71
$E_{oed}^{ref}$	176.92
$E_{oed}^{ref} \times 2.0$	210.59
$E_{oed}^{ref} \times 4.0$	354.60

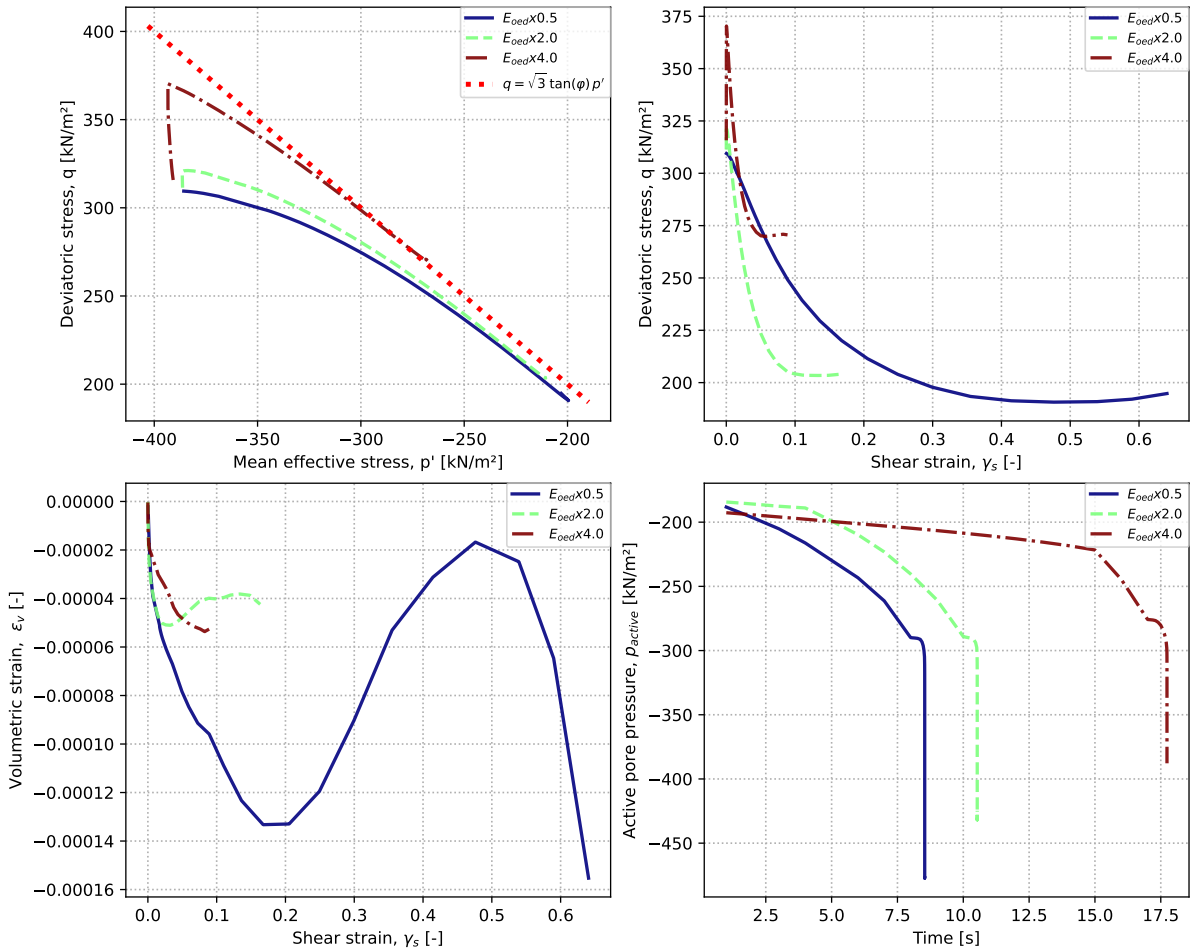


FIGURE 10. Direct shear stress path at a slip surface point for different compressibilities, throughout the triggering assessment. As compressibility increases, the material exhibits reduced volumetric deformation and requires more time to develop sufficient pore water pressure to trigger flow-liquefaction failure. Moreover, HSsmall exhibits a strong limitation in the fully coupled context, where less compressible materials exhibit more brittle behavior; at the same time, they require higher triggering loads to develop pore water pressures and form a slip surface.

787 **4.6. Influence of Tailings Compressibility on Diffuse Localization bandwidth.** We seek to assess  
 788 the influence of tailings compressibility on the localization bandwidth and triggering response. Thus, we  
 789 scale the stiffness parameters  $E_{oed}^{ref}$ ,  $E_{ur}^{ref}$ ,  $E_{50}^{ref}$ , and  $G_0^{ref}$  listed in Table 1 by a common factor. This  
 790 approach modifies the material's overall compressibility while preserving its peak and residual strengths  
 791 by proportionally adjusting the strains at which these occur (Sottile et al., 2020). The baseline scenario  
 792 corresponds to the TSF model run at a loading rate of  $r = 0.02$  kPa/s, as presented in the previous  
 793 section.

794 Table 6 summarizes the resulting trigger loads for different oedometric stiffness values. The results  
 795 show a clear trend: as stiffness increases (i.e., as compressibility decreases), the trigger load rises. This  
 796 inverse relationship indicates that more compressible materials, which allow greater volumetric deforma-  
 797 tion under loading, are more susceptible to premature failure.

798 Figure 9 illustrates how this behavior manifests in the deformation field. Consistent with the analytical  
 799 scaling relation derived in Section 3.2 for the induced shear bandwidth, the simulations show that more  
 800 compressible materials form narrower and more localized shear bands, while stiffer materials distribute  
 801 deformation over wider regions. The corresponding pore-pressure fields exhibit a similar pattern: higher  
 802 compressibility enhances pore-pressure accumulation within localized zones, reinforcing the link among  
 803 diffusion capacity, compressibility, and the spatial extent of deformation.

804 Figure 10 shows the stress–strain and time–evolution data. This data is taken at a representative point  
 805 along the developing slip surface. The  $q$ – $p'$  diagram reveals that stiffer materials exhibit a pronounced  
 806 initial strength increase before converging towards the direct simple shear failure line,

$$q = \sqrt{3} \tan \phi p',$$

807 where  $\phi$  is the material friction angle. This initial strength gain results from reduced volumetric com-  
 808 pressibility, as indicated by the shear strain–volumetric strain relation, which in turn delays the buildup  
 809 of pore pressure during loading. The time versus pore pressure response confirms this interpretation:  
 810 stiffer materials dissipate pressure gradients more effectively, whereas more compressible ones experience  
 811 rapid pore-pressure rise and earlier loss of effective stress.

812 **Remark 5. Limitations of HSsmall for Fully-Coupled Flow-Liquefaction Triggering-Load**  
 813 **Predictions.** *The shear strain–deviatoric stress response also exposes a limitation of the HSsmall model*  
 814 *when applied to flow-liquefaction problems in a fully coupled framework. The model predicts increasingly*  
 815 *brittle behavior for stiffer (less compressible) materials, leading to unrealistic post-peak responses incon-*  
 816 *sistent with experimental evidence (Jefferies and Been, 2016b; Smith et al., 2019; Tasso et al., 2026). As*  
 817 *a consequence, this artifact can result in artificially high trigger loads in materials that, in reality, would*  
 818 *undergo more ductile pore-pressure driven softening and progressive failure. Therefore, while HSsmall*  
 819 *provides valuable insight into stiffness-dependent trends, its application to brittle or highly contractive*  
 820 *tailings should be exercised with caution, and future work should consider alternative constitutive formu-*  
 821 *lations that better capture the interplay between compressibility, dilatancy, and pore-pressure generation*  
 822 *in liquefiable materials.*

823

## 5. CONCLUSIONS

824 This study shows that fully coupled hydro–mechanical formulations possess an inherent, physically  
 825 grounded regularization mechanism absent in purely mechanical or uncoupled models. By coupling  
 826 momentum balance with pore-fluid diffusion, the governing equations naturally impose a diffuse finite  
 827 localization bandwidth that limits the growth of pore-pressure driven strain-softening instabilities. This  
 828 internal length scale arises from the combined effects of material and hydraulic properties—permeability,  
 829 fluid compressibility, and solid-skeleton stiffness—and their interaction with the effective diffusivity and  
 830 numerical parameters such as the time step, load increment, and loading rate. Together, these factors  
 831 define the system’s capacity to redistribute pore pressures and modulate deformation.

832 Numerical stability is achieved only when mesh resolution and time increments are consistent with  
 833 this diffusion-driven length scale. Under such conditions, simulations yield mesh-independent predictions  
 834 of both liquefaction initiation and post-trigger evolution. The spectral stability analysis establishes a  
 835 clear dispersion relation governing perturbation growth: short-wavelength modes decay when the time  
 836 step exceeds a critical threshold, effectively filtering out non-physical instabilities. Numerical triaxial  
 837 simulations confirm this analytical prediction. For sufficiently large increments, deformation localises  
 838 into single, physically consistent shear bands, and the stress–strain response becomes insensitive to mesh  
 839 refinement. Conversely, smaller time steps permit the persistence of high-frequency modes, causing  
 840 element-scale banding and premature pore-pressure driven softening. The comparison between coupled  
 841 and uncoupled formulations reveals that pore-pressure diffusion plays a crucial redistributive role: it  
 842 suppresses local overstressing, aligns Gauss-point stress trajectories with the macroscopic response, and  
 843 ensures a smooth post-peak transition. In contrast, uncoupled models exhibit unrestrained pore-pressure  
 844 driven softening and spurious unloading, resulting in non-unique and mesh-dependent outcomes.

845 At the tailings-storage-facility (TSF) scale, the same stabilizing mechanism governs system-wide be-  
 846 havior. Parametric analyses confirm that decreasing permeability systematically narrows localization  
 847 bands and lowers triggering loads, driving the material response toward an asymptotic undrained regime.  
 848 The coupled formulation naturally captures this transition, seamlessly linking drained, partially drained,

849 and undrained responses without the need for artificial boundary constraints. The interaction between  
 850 load rate and increment size further refines the interpretation: rapid loading accelerates pore-pressure  
 851 accumulation, producing narrow, sharply defined bands, while larger increments act as diffusive filters  
 852 that widen the deformation zone and damp short-wave fluctuations. This load-rate/increment-size rela-  
 853 tionship establishes a clear physical connection between hydraulic diffusivity, deformation morphology,  
 854 and liquefaction susceptibility across scales. The relationships identified between permeability, load-  
 855 ing rate, and diffuse localization width should be interpreted as mechanistic scaling results emerging  
 856 from the coupled governing equations, rather than as empirical correlations calibrated against specific  
 857 experimental or field case histories.

858 Therefore, two major conclusions arise from these findings. First, fully coupled hydro–mechanical  
 859 formulations provide a *physical*, rather than numerical, pathway to regularization. The diffusion terms  
 860 embedded in the governing equations impose intrinsic length and time scales that restore uniqueness  
 861 and ensure predictive reliability in liquefaction analyses. Second, they underscore the importance of  
 862 numerical consistency: mesh size, time step, and load increments must be consistent with the problem’s  
 863 diffusion-controlled scales. When properly selected, these parameters enable robust, mesh-independent  
 864 solutions that accurately reproduce both laboratory and field-scale behaviour. Within this quasi-static  
 865 setting, the diffusion-driven regularization and the associated scaling relationships are not contingent  
 866 upon the specific constitutive model adopted, provided that a consistent constitutive tangent operator  
 867 exists for the linearization of the governing equations.

868 By integrating analytical insight, controlled triaxial simulations, and TSF-scale modelling, we ob-  
 869 tain a coherent and verifiable framework for predicting liquefaction triggers and post-failure evolution.  
 870 The results highlight that drained, partially drained, and undrained responses emerge not as imposed  
 871 conditions but as natural outcomes of the coupled equations, governed by permeability, load rate, and  
 872 boundary configuration. This unified perspective bridges theory and practice, providing a physically  
 873 consistent basis for evaluating tailings dam stability and the mechanisms underlying flow liquefaction.

874 Future research will incorporate advanced constitutive models—particularly critical-state or  
 875 anisotropic plasticity formulations—to capture progressive failure and post-liquefaction deformation more  
 876 realistically. Large-scale applications should also investigate the combined influence of staged construc-  
 877 tion, hydraulic barriers, and spatial heterogeneity in permeability to assess system-wide liquefaction  
 878 susceptibility. These developments would expand the predictive scope of fully coupled analyses and  
 879 strengthen their integration into practical dam safety assessment and design, ensuring that the coupling  
 880 between hydraulic and mechanical processes is faithfully represented across scales.

## 881 REFERENCES

- 882 Z. P. Bažant and B.-H. Oh. Crack band theory for fracture of concrete. *Materials and Structures*, 16(3):  
 883 155–177, 1983. doi: 10.1007/BF02486267. URL [https://link.springer.com/article/10.1007/  
 884 BF02486267](https://link.springer.com/article/10.1007/BF02486267).
- 885 R. B. J. Brinkgreve, S. Kumarswamy, W. M. Swolfs, E. Engin, F. Fonseca Arévalo, N. Ragi Manoj,  
 886 L. Zampich, and N. Zalamea. *PLAXIS Connect Edition V20.03 Manuals*. Bentley Systems, Delft, The  
 887 Netherlands, 2020. User and Reference Manuals for PLAXIS CONNECT Edition (V20.03).
- 888 CIMNE/UPC. Computational analysis of the failure of dam i at the córrego do feijão mine (brumadinho):  
 889 Final technical report. Technical report, International Centre for Numerical Methods in Engineering  
 890 (CIMNE) and Universitat Politècnica de Catalunya (UPC), Barcelona, Spain, oct 2021. Final technical  
 891 report submitted to the Brazilian Federal Prosecutor’s Office (MPF), with independent technical  
 892 oversight.
- 893 Olivier Coussy. *Poroviscoelasticity*, chapter 9, pages 261–277. John Wiley and Sons, Ltd, 2003. ISBN  
 894 9780470092712. doi: <https://doi.org/10.1002/0470092718.ch9>. URL [https://onlinelibrary.wiley.  
 895 com/doi/abs/10.1002/0470092718.ch9](https://onlinelibrary.wiley.com/doi/abs/10.1002/0470092718.ch9).
- 896 Wenjie Cui, Xiaotian Wu, David M. Potts, and Lidija Zdravković. Nonlocal strain regularisation for  
 897 critical state models with volumetric hardening. *Computers and Geotechnics*, 157:105350, 2023. doi:  
 898 10.1016/j.compgeo.2023.105350.
- 899 F. Darve and F. Laouafa. Instabilities in granular materials and application to landslides. *Mechanics of*  
 900 *Cohesive-frictional Materials*, 5(8):627–652, 2000.
- 901 Félix Darve, Luc Sibille, Ali Daouadji, and François Nicot. Bifurcations in granular media: macro- and  
 902 micro-mechanics approaches. *Comptes Rendus Mécanique*, 335(9):496–515, 2007. ISSN 1631-0721.  
 903 doi: <https://doi.org/10.1016/j.crme.2007.08.005>. URL [https://www.sciencedirect.com/science/  
 904 article/pii/S1631072107001398](https://www.sciencedirect.com/science/article/pii/S1631072107001398). Joseph Boussinesq, a Scientist of bygone days and present times.

- 905 Eduardo A. de Souza Neto, Djordje Perić, and David R. J. Owen. *Computational Methods for Plasticity: Theory and Applications*. Wiley, Chichester, 2008. ISBN 978-0-470-69452-7.
- 906 G. Duvaut and J.-L. Lions. *Inequalities in Mechanics and Physics*. Grundlehren der Mathematischen Wissenschaften. Springer, Berlin, Heidelberg, 1976. ISBN 978-3-642-66165-5. doi: 10.1007/978-3-642-66165-5. URL <https://link.springer.com/book/10.1007/978-3-642-66165-5>.
- 907 908 909 910 K. Bernardo M. Sottile A Sfriso F. Lopez Rivarola, N. Tasso. Evaluation of triggering of static liquefaction of tailings dams considering the swcc. *Mine Waste and Tailings Conference 2023, Brisbane, Australia, 2023*.
- 911 912 Eleni Gerolymatou, Alexandros Stathas, and Ioannis Stefanou. Do multiphysics processes lead to mesh independent analyses? *International Journal of Mechanical Sciences*, 274:109265, 2024. doi: 10.1016/j.ijmecsci.2023.109265.
- 913 914 915 Anders Samstad Gylland, Hans Petter Jostad, and Steinar Nordal. Experimental study of strain localization in sensitive clays. *Acta Geotechnica*, 8(4):369–379, 2013. doi: 10.1007/s11440-013-0217-8.
- 916 917 Michael Jefferies, Norbert R. Morgenstern, Dirk V. Van Zyl, and John Wates. Report on ntsf embankment failure, cadia valley operations, for ashurst australia. Technical report, International Centre for Numerical Methods in Engineering (CIMNE), April 2019.
- 918 919 920 Mike Jefferies and Ken Been. *Soil Liquefaction: A Critical State Approach*. CRC Press, Boca Raton, FL, 2 edition, 2016a. ISBN 9780367873400.
- 921 922 923 Mike Jefferies and Ken Been. *Soil Liquefaction: A Critical State Approach*. CRC Press, Boca Raton, FL, 2 edition, 2016b.
- 924 925 Milan Jirásek and Zdeněk P. Bažant. *Inelastic Analysis of Structures*. John Wiley & Sons, Chichester, 2002. ISBN 9780471987161.
- 926 927 Takeshi Kodaka, Yosuke Higo, Sayuri Kimoto, and Fusao Oka. Effects of sample shape on the strain localization of water-saturated clay. *International Journal for Numerical and Analytical Methods in Geomechanics*, 31(4):483–521, 2007. doi: 10.1002/nag.585.
- 928 929 930 Tetsuya Kodaka, Yuki Higo, and Tatsuya Takyu. Deformation and failure characteristics of rectangular clay specimens under three-dimensional condition. In *Proceedings of an International Conference on Geomechanics*, Kyoto, Japan, 2005. IOS Press / Millpress.
- 931 932 Osvaldo Ledesma, Alejo Sfriso, and Diego Manzanal. Procedure for assessing the liquefaction vulnerability of tailings dams. *Computers and Geotechnics*, 144:104632, 2022.
- 933 934 Miguel A. Mánica, Antonio Gens, Jacques Vaunat, and Diego F. Ruiz. Nonlocal plasticity modelling of strain localisation in stiff clays. *Computers and Geotechnics*, 103:138–150, 2018. doi: 10.1016/j.compgeo.2018.07.008. URL <https://www.sciencedirect.com/science/article/pii/S0266352X18301733>.
- 935 936 937 938 Miguel A. Mánica, Marcos Arroyo, Antonio Gens, and Luis Monforte. Application of a critical state model to the merriespruit tailings dam failure. *Proceedings of the ICE – Geotechnical Engineering*, 175, 2021. doi: 10.1680/jgeen.21.00001.
- 939 940 941 Norbert R. Morgenstern, Steven G. Vick, and Dirk V. Van Zyl. Report on mount polley tailings storage facility breach. Technical report, Independent Expert Engineering Investigation and Review Panel, Province of British Columbia, Canada, 2015. URL <https://www.mountpolleyreviewpanel.ca/sites/default/files/report/ReportonMountPolleyTailingsStorageFacilityBreach.pdf>.
- 942 943 944 945 H. B. Mühlhaus and E. C. Aifantis. A variational principle for gradient plasticity. *International Journal of Solids and Structures*, 28(7):845–857, 1991. doi: 10.1016/0020-7683(91)90004-Y. URL <https://www.sciencedirect.com/science/article/pii/002076839190004Y>.
- 946 947 948 Roberto Nova. Controllability of the incremental response of soil specimens subjected to arbitrary loading programmes. *Journal of the Mechanical Behavior of Materials*, 5(2):193–202, 1994.
- 949 950 Roberto Nova and Tomasz Hueckel. A unified approach to the modelling of liquefaction and cyclic mobility of sands. *Soils and Foundations*, 21(4):13–28, 1981. ISSN 0038-0806. doi: <https://doi.org/10.3208/sandf1972.21.4.13>. URL <https://www.sciencedirect.com/science/article/pii/S0038080620325002>.
- 951 952 953 954 Fumio Oka, Tetsuya Kodaka, Shun-ichi Kimoto, Tetsuya Ichinose, and Yuki Higo. Strain localization of rectangular clay specimen under undrained triaxial compression conditions. In *Proceedings of the 16th International Conference on Soil Mechanics and Geotechnical Engineering*, Amsterdam, 2006. Millpress Science Publishers / IOS Press. doi: 10.3233/978-1-61499-656-9-841.
- 955 956 957 958 Fusao Oka and Sayuri Kimoto. *Computational Modeling of Multiphase Geomaterials*. CRC Press, London, 1 edition, 2012. ISBN 9780429088872. doi: 10.1201/b12273.
- 959 960 P. Perzyna. Fundamental problems in viscoplasticity. In W. Flügge and C. Truesdell, editors, *Advances in Applied Mechanics*, volume 9, pages 243–377. Academic Press, 1966. doi: 10.1016/S0065-2156(08)

- 963 70009-7. URL <https://www.sciencedirect.com/science/article/pii/S0065215608700097>.
- 964 Klaus Regenauer-Lieb, Manman Hu, Qingpei Sun, Chong Liu, Zhennan Zhu, and Victor Calo. A thermo-  
965 dynamic framework for turing-type instabilities in deforming porous media: Part I Theory. –, 2025a.  
966 Draft. Awaiting submission.
- 967 Klaus Regenauer-Lieb, Manman Hu, Qingpei Sun, Chong Liu, Zhennan Zhu, and Victor Calo. A ther-  
968 modynamic framework for turing-type instabilities in porous media: Part II Applications. –, 2025b.  
969 Draft. Awaiting submission.
- 970 F. Lopez Rivarola and N. Tasso. Analysis of flow liquefaction triggering in tailings dams consider-  
971 ing coupled flow-deformation. *Proceedings of the 17th Pan-American Conference on Soil Mechanics*  
972 *and Geotechnical Engineering (XVII PCSMGE), and 2nd Latin-American Regional Conference of the*  
973 *International Association For Engineering Geology and the Environment (IAEG), La Serena Chile,*  
974 *2024.*
- 975 Laura A. Rødvand, Hans Petter Jostad, Gustav Grimstad, and Lars Andresen. Modelling mesh inde-  
976 pendent failure loads of a soft strain-softening clay using a rate dependent model. *Computers and*  
977 *Geotechnics*, 161:105265, 2023. PII: S0266-352X(23)002690; preprint/open version available at NTNU  
978 Open.
- 979 Erick Rógenes, Ian Torras Paes, Bruno Guimarães Delgado, Rafael Jabur Bittar, Alessandra dos San-  
980 tos Gomes, Alessandro Cirone, Alomir H. Fávero Neto, and Leandro Lima Rasmussen. Assessing static  
981 liquefaction triggers in tailings dams using the critical state constitutive models CASM and NorSand.  
982 *International Journal for Numerical and Analytical Methods in Geomechanics*, 49(4):1092–1112, De-  
983 cember 2024. ISSN 0363-9061. doi: 10.1002/nag.3914. URL [https://onlinelibrary.wiley.com/](https://onlinelibrary.wiley.com/doi/10.1002/nag.3914)  
984 [doi/10.1002/nag.3914](https://onlinelibrary.wiley.com/doi/10.1002/nag.3914).
- 985 John W. Rudnicki and James R. Rice. Conditions for the localization of deformation in pressure-  
986 sensitive dilatant materials. *Journal of the Mechanics and Physics of Solids*, 23(6):371–394, 1975. doi:  
987 10.1016/0022-5096(75)90003-5.
- 988 Bernhard Schrefler, Carmelo Majorana, and Lorenzo Sanavia. Shear band localization in saturated  
989 porous media. *Archives of Mechanics*, 47:577–599, 01 1995.
- 990 Babak Shahbodagh, Dunja Perić, and Nasser Khalili. Effects of stress histories and drainage conditions  
991 on inception of strain localization in unsaturated soils. *Computers and Geotechnics*, 156:105291, 2023.  
992 doi: 10.1016/j.compegeo.2022.105291.
- 993 Kyle Smith, Riccardo Fanni, Peter Chapman, and David Reid. Critical state testing of tailings: com-  
994 parison between various tailings and implication for design. *Proceedings of Tailings and Mine Waste,*  
995 *Vancouver, Canada*, pages 1–12, 2019.
- 996 M. Sottile, I. Cueto, and A. Sfriso. A simplified procedure to numerically evaluate triggering of static  
997 liquefaction in upstream-raised tailings storage facilities. In *Proceedings of COBRAMSEG*, Campinas,  
998 2020.
- 999 Mauro G. Sottile, Nicolás A. Labanda, Alejandro Kerguelén, Ignacio A. Cueto, and Alejo O. Sfriso.  
1000 Stability assessment of a tailings storage facility using a non-local constitutive model accounting for  
1001 anisotropic strain-softening. In Marco Barla, Alice Di Donna, and Donatella Sterpi, editors, *Challenges*  
1002 *and Innovations in Geomechanics. IACMAG 2021*, volume 126 of *Lecture Notes in Civil Engineering*,  
1003 pages 334–342, Cham, 2021. Springer. ISBN 978-3-030-64517-5. doi: 10.1007/978-3-030-64518-2\_40.  
1004 URL [https://doi.org/10.1007/978-3-030-64518-2\\_40](https://doi.org/10.1007/978-3-030-64518-2_40).
- 1005 Jean Sulem and Ioannis Vardoulakis. *Bifurcation Analysis in Geomechanics*. Chapman and Hall / CRC  
1006 Press, London, 1995. ISBN 9780412567401. doi: 10.1201/9781482269383.
- 1007 N. Tasso, F. Lopez Rivarola, O. De Santiago, N. Rivas, and M. Sottile. Calibration constitutive models for  
1008 flow liquefaction: a word of caution. *First International Symposium of Tailings Deposits, Chihuahua,*  
1009 *Mexico*, 2024.
- 1010 Nicolas Tasso, Nicolas Labanda, Kuntan Chang, and Riccardo Fanni. Gold tailings database: parameters’  
1011 variability and correlations. *Proceedings of the 21st International Conference on Soil Mechanics and*  
1012 *Geotechnical Engineering, Vienna, Austria*, 2026. Approved. Awaiting for publication.
- 1013 J. G. M. Vermeer and R. de Borst. Non-associated plasticity for soils, concrete and  
1014 rock. *Heron*, 29(3):1–64, 1984. URL [https://repository.tudelft.nl/record/uuid:](https://repository.tudelft.nl/record/uuid:4ee188ab-8ce0-4df3-adf5-9010ebfaabf0)  
1015 [4ee188ab-8ce0-4df3-adf5-9010ebfaabf0](https://repository.tudelft.nl/record/uuid:4ee188ab-8ce0-4df3-adf5-9010ebfaabf0).
- 1016 H. W. Zhang, L. Sanavia, and B. A. Schrefler. An interal length scale in dynamic strain localization of  
1017 multiphase porous media. *Mechanics of Cohesive-frictional Materials*, 4(5):443–460, 1999.
- 1018 O. C. Zienkiewicz, A. H. C. Chan, M. Pastor, D. K. Paul, and T. Shiomi. Static and dynamic behaviour  
1019 of soils: a rational approach to quantitative solutions. i. fully saturated problems. *Proceedings of the*  
1020 *Royal Society of London. Series A*, 429(1877):285–309, 1990.

- 1021 Olek C. Zienkiewicz, A. H. C. Chan, Manuel Pastor, Bruno A. Schrefler, and Tetsuya Shiomi. *Com-*  
1022 *putational Geomechanics with Special Reference to Earthquake Engineering*. John Wiley & Sons,  
1023 Chichester, 1999.